SLAC-PUB-5177
February 1990
(A)

BUNCH LENGTHENING IN THE SLC DAMPING RINGS*

KARL L. F. BANE

Stanford Linear Accelerator Center
Stanford University, Stanford, California 94309

Contributed to the Impedance and Bunch Instability Workshop
Advanced Photon Source, Argonne, Illinois, October 31–November 1, 1989.

* Work supported by Department of Energy contract DE–AC03–76SF00515.

TABLE OF CONTENTS

1. INTRODUCTION

A high level of current dependent bunch lengthening has been observed on the North damping ring of the Stanford Linear Collider (SLC).[1] At currents of 3 x 10^{10} this behavior does not appear to degrade the machine's performance significantly. However, at the higher currents that are envisioned for the future one fears that its performance could be greatly degraded due to the phenomenon of bunch lengthening. This was the motivation for the work described in this paper.

In Chapter 2 we calculate the longitudinal impedance of the damping ring vacuum chamber. More specifically, in this chapter we find the response function of the ring to a short Gaussian bunch, which we call the Green function wake. In addition, we try to estimate the relative importance of the different vacuum chamber objects, in order to see how we might reduce the ring impedance. Chapter 3 describes bunch length measurements performed on the North damping ring. In Chapter 4, we use the Green function wake, discus-sed above, to compute the bunch lengthening. Then we compare these results with those obtained from the measurements. In addition, in this chapter we calculate the current dependence of the tune distribution. Note that each of these chapters is based on work already described in a published report: Chapter 2 in "The Calculated Longitudinal Impedance of the SLC Damping Rings" by K. Bane, Ref. (2), Chapter 3 in "Bunch Lengthening in the SLC Damping Ring" by L. Rivken ***et al.,*** Ref. (1), and Chapter 4 in "Bunch Lengthening Calculations for the SLC Damping Rings" by K. Bane and R. Ruth, Ref. (3). The only completely new work is the tune calculations.

2. THE CALCULATED LONGITUDINAL IMPEDANCE

2.1 Introduction

The SLC damping ring vacuum chamber contains many small discontinuities—such as shallow steps, transitions, masks, and bellows-as well as larger objects like the beam position monitors and the rf cavities. In this chapter we study the relative importance of the various objects to the total ring impedance. In addition,

we obtain a Green function that will be used in a later chapter for bunch length calculations.

In this paper we are interested only in the single bunch effects of the vacuum chamber impedance. The true vacuum chamber impedance is normally very complicated, containing many resonances and other structure, and covers a wide frequency range. A single bunch, however, only probes the impedance after it has been smoothed by the bunch spectrum, the so-called "broad-band impedance." The time domain correspondent to this impedance is the short range wakefield.

In this paper, we choose to work in the time domain, and all our results are based on wakefield computations. Consider an infinitely long tube which at some position is momentarily interrupted by a cavity, an obstruction, or other change in cross-section. Now consider a bunch of electrons (or positrons) passing at the speed of light c parallel to the-axis of the pipe, from minus to plus infinity. The longitudinal wakefield W(t), then, is defined as the total voltage-divided by the charge in the bunch-gained by a test particle that has followed the same path, also at velocity c, but at relative position ***ct.*** We will use the convention that a more negative value of time *t* is more toward the front of the bunch. In most of the cases that we consider the structure geometry is cylindrically symmetric, and we use T. Weiland's computer program TBCI[4] to calculate the wakefield. Note that by limiting our structures to those with equal beam pipes we force the system's potential energy at the beginning of the calculation to be the same as at the end.

2.2 Types of Impedances

2.2.1 ***Introduction***

A vacuum chamber object in a storage ring can be described as inductive, resistive, or capacitive, depending upon whether it tends to cause bunch lengthening, bunch shortening, or does not affect the bunch length. We can discern which of these catagories applies to an object from the shape of the voltage that it induces. We can further speak of a vacuum chamber object as being a good-or

ideal-inductor, resisitor, or capacitor if its induced voltage is related to the driving current in a manner analogous to that found in the corresponding simple circuit element. It is important to note, however, that in either case the applicability of the terms inductive, resistive, or capacitive depends not only on the shape of the object itself, but also on the length of the exciting bunch. As the bunch length changes different parts of the object's impedance become emphasized. Normally, vacuum chamber objects appear more inductive to longer bunches, more capacitive to-shorter bunches.

2.2.2 Inductive Objects

If the effective slope of the induced voltage opposes the slope of the rf wave then the object is inductive, and it will tend to lengthen the bunch. We denote as good inductors objects for which the induced voltage can be approximated by $V_{ind} = -L\,dI/dt$ with the constant L the inductance and I the bunch current. We note that this model, in detail, is unphysical: it predicts that the beam loses no energy passing by the object. If the induced voltage of a vacuum chamber object is well approximated by the above relation, it means that the beam sees primarily the low frequency part of the object's impedance; and that in this region the impedance is purely imaginary, and linear with a slope of $-L$. Note that if an object is a good inductor at a certain bunch length, it will continue to be so at longer bunch lengths.

It is often easy to see whether or not an object is a good inductor for a Gaussian bunch with length σ. Normally, inductive objects tend to be small discontinuities. Now suppose we have a small obstruction in a tube of radius a. If the bunch length obeys the relation $\sigma \gtrsim a/2$ then little of its power spectrum ($\lesssim 9\%$) is above the tube cut-off frequency. When the beam passes by the obstruction it will therefore leave little energy behind, since the tube will not support free waves below its cut-off. The head of the beam will lose energy to the discontinuity, but the tail will reabsorb most of it, resulting in an inductive wakefield. In the SLC damping rings there are many small discontinuities on tubes of radius 11 mm (or less) which,

according to the above criterion, are good inductors for bunch lengths down to 5.5 mm. Note that since only for the tails of the beam's spectrum-at frequencies above the tube cut-off-is the real part of the impedance nonzero, the higher mode loss that we do find in inductors decreases exponentially fast as the bunch length is increased.

Objects that can be considered good inductors for bunch lengths normally found in storage rings are shallow transitions, shallow cavities, bellows, masks, or bumps in the vacuum chamber walls. We shall see that the SLC damping ring contains many such objects, which therefore define the character of its impedance. As an example of a good inductor Fig. l(b) displays the shape of a QD bellows of the SLC damping rings. The wakefield of a 6 mm Gaussian beam passing by this object, as calculated by TBCI, is shown in Fig. l(a). The beam shape is represented by the dotted curve, with the front to the left. Note that in our convention the slope of the applied rf must be negative for machines operating above transition.

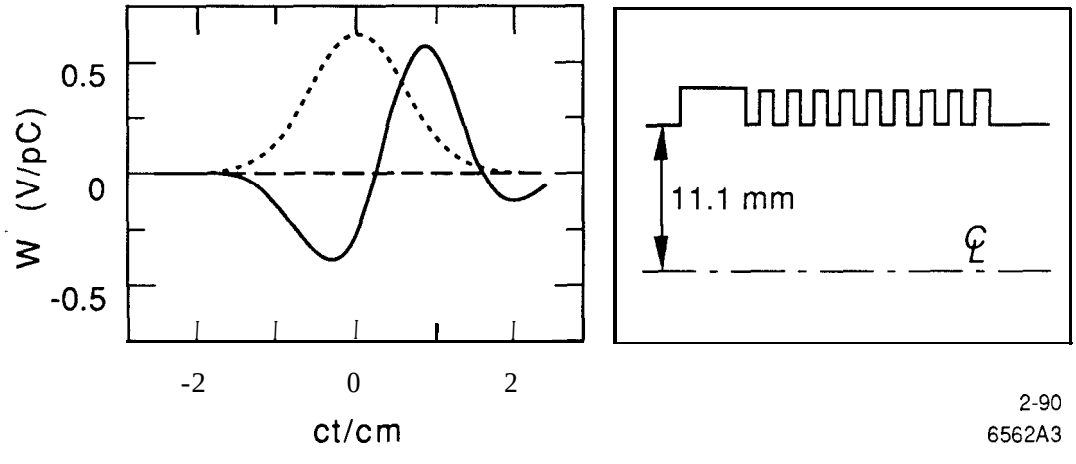

Fig. 1. An inductive example: the wakefield of a 6 mm Gaussian bunch passing by the QD bellows of the SLC damping ring.

2.2.3 Resistive Objects

If the effective slope of the induced voltage is almost zero then the object is resistive, and it has little effect on bunch lengthening. We denote as good resistors

objects for which the induced voltage ca be approximated by $V_{ind} = -IR$, with the constant R the resistance. We note that this model is also not strictly physical: since these beams are assumed to be moving at the speed of light, the induced voltage must lag, even if by a slight amount, behind the driving current. Note that for good resistors the loss factor-the total higher mode loss divided by the bunch charge-is approximated by $k = R/(2\sqrt{\pi}\sigma)$. Examples of good resistive elements found in storage rings are deep cavities, such as the rf cavities, for bunches that are not short compared to the beam tubes. As resistive example Fig. 2(a) shows the wakefield left by a 6 mm Gaussian bunch passing by one of the two 2-cell rf cavities of the SLC damping rings [Fig. 2(b) displays the shape of one cell].

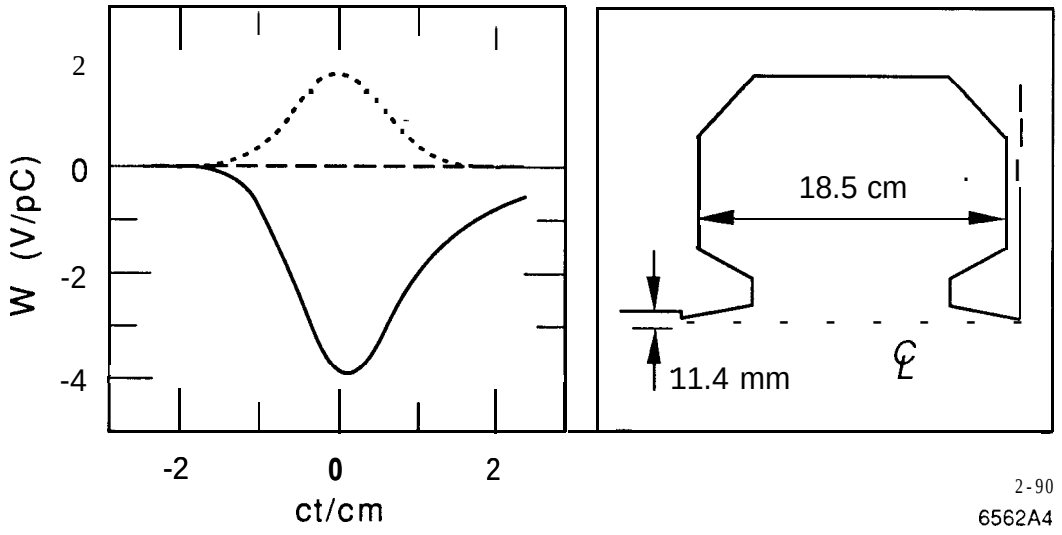

Fig. 2. A resistive example: the wakefield of a 6 mm Gaussian bunch passing by one of the rf cavities of the SLC damping ring.

2.2.4 Capacitive Objects

Finally, if the effective slope of the induced voltage enhances the rf slope then the object is capacitive, and it will tend to shorten the bunch. We denote as good capacitors objects for which the induced voltage is approximately proportional to the integral of the current, with constant of proportionality -l/C, and C the

capacitance. This model is strictly unphysical in that it predicts that the energy loss of a bunch depends only on the total charge of the beam, and not on the peak current. This type, of the three types of objects, is probably the least commonly encountered in storage rings. Reference (5) describes a capacitive device, the so-called "SPEAR capacitor," that was installed in a ring for the specific purpose of shortening the bunch. The wakefield of very short bunches in deep cavities falls somewhere between that of a pure resistor and a pure capacitor. The rf cavity of -Fig. 2 can be considered slightly capacitive in that the average slope of the induced voltage is slightly negative. However, there are no very capacitive objects in the SLC damping rings. But to give an example of a fairly good capacitor, we show in Fig. 3(a) the wakefield of a 6 mm Gaussian bunch passing by the cavity of Fig. 3(b).

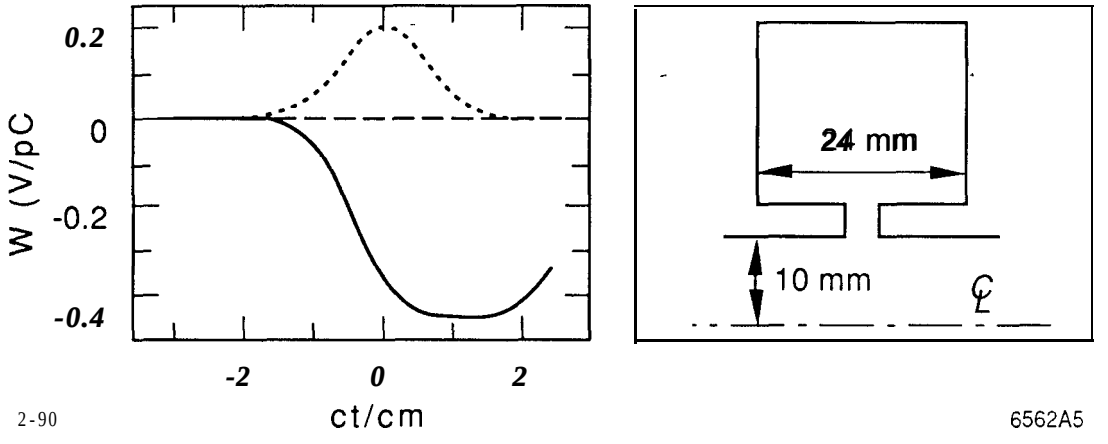

Fig. 3. A capacitive example: the wakefield of a 6 mm Gaussian bunch passing by the structure shown at right.

2.3 The Effective Inductance

The loss factor ***k*** is often used to estimate the contribution of an object to the ring impedance. This parameter gives the higher mode losses of the object but says little about its contribution to bunch lengthening. Alternatively, we can say that it is a measure of the real, not the imaginary, part of the impedance. As a

figure of merit that is a complement to the loss factor, and that is a measure of the imaginary part of the impedance, we will use the effective inductance ℓ.

Recall that the loss factor is given by the average value of the wakefield along the bunch

$$k = -\int_{-\infty}^{\infty} W(t)\lambda(t)\,dt = \int_{-\infty}^{\infty}\left[\int_{0}^{\infty} W_\delta(t')\lambda(t-t')\,dt'\right]\lambda(t)\,dt \quad , \tag{1}$$

with λ the longitudinal charge distribution and W_δ the Green function (or delta function) wake. The Green function, in turn, is given by the inverse Fourier transform of the impedance Z:

$$W_\delta(t) = \frac{1}{2\pi}\int_{-\infty}^{\infty} Z(\omega)e^{-i\omega t}\,d\omega \quad , \tag{2}$$

with w the frequency. Therefore, the loss factor c-an also be written in terms of the impedance as

$$k = \frac{1}{\pi}\int_{0}^{\infty} X(\omega)|\tilde{\lambda}(\omega)|^2\,d\omega \quad , \tag{3}$$

with $\tilde{\lambda}$ the Fourier transform of the charge distribution and X the real part of Z. Thus k gives the real part of the impedance averaged over the square of the bunch spectrum.

Let us define the effective inductance ℓ by the following operation: We compute the wakefield for a Gaussian bunch and then perform a least squares fit to

$$W(t) = -\ell\frac{d\lambda(t)}{dt} \quad . \tag{4}$$

Therefore ℓ can be written in terms of the impedance as

$$\ell = -\int_{0}^{00} Y(\omega)|\tilde{\lambda}(\omega)|^2\omega\,dw \Big/ \int_{0}^{\infty}|\tilde{\lambda}(\omega)|^2\omega^2\,d\omega \quad , \tag{5}$$

with Y the imaginary part of Z. We see that e-up to a bunch length factor-is the product of Yw averaged over the square of the bunch spectrum. For a pure inductance, $Z = -i\omega L$, we see that ℓ reduces to L. For a Gaussian beam Eq. (5) becomes

$$\ell = \frac{4\sigma^3}{\sqrt{\pi}} \int Y(\omega) e^{-\omega^2\sigma^2} \omega \, d\omega \quad . \tag{6}$$

Note that, as in Ref. (5), we might alternatively have chosen as figure of merit the bunch length times the average slope of the wake:

$$\alpha = \sigma \int_{-\infty}^{\infty} W'(t)\lambda(t) \, dt = 2\sigma \int_{0}^{\infty} Y(\omega)|\tilde{\lambda}(\omega)|^2 \omega \, dw \ . \tag{7}$$

We see-that α—up to a bunch length factor-is the same as ℓ. As a fine point, we also note that in the results to-be presented a Gaussian weighting factor has been included in the least squares calculations that determine ℓ. Therefore, instead of by Eq. (6), ℓ will be given by

$$\ell = -\frac{3}{2}\sqrt{\frac{3}{\pi}} \int_{0}^{\infty} Y(\omega) e^{-3\omega^2\sigma^2/4} \omega \, d\omega \quad . \tag{8}$$

2.4 Some Simple Inductors

Let us consider the simple discontinuities of Fig. 4. To a Gaussian bunch sufficiently long (i.e., one with length σ greater than half the tube radius) they will appear as good inductors. For each of the three models we have performed parametric studies to find its inductance. To obtain a data point, we first computed the wakefield of a reasonably long Gaussian bunch passing by the structure in question, using TBCI. Then, we performed a least squares fit to Eq. (4), weighted by the Gaussian bunch shape, in order to obtain the effective inductance ℓ. And finally we found the limiting value of ℓ, as σ becomes large, which we take as the inductance L of the object.

In order to reduce our work we computed the wakefield in the following manner: We first performed a TBCI calculation for a short Gaussian bunch of length σ_1, calculating the wakefield to a long distance behind the driving bunch. Given this wakefield W_1, we then obtained the wakefield for longer bunches, with length σ, by performing the following integration[6]:

$$W(t) = \frac{}{} \int_{-\infty}^{\infty} W_1(t') \exp\left[-\frac{(t-t')^2}{2\sigma_t^2}\right] dt' \quad (\quad a \quad > \sigma_1) , \tag{9}$$

with $\sigma_t^2 = \sigma^2 - \sigma_1^2$. In this way, for any given structure, one TBCI calculation provides the wakefield for Gaussians over a wide range of bunch lengths.

We began our studies with the small cavity, shown in Fig. 4(a). It is interesting to note that the numerical results we obtained for it can be well approximated by a simple application of Faraday's Law. According to Faraday's Law the voltage induced across the gap depends on the time rate of change of the magnetic flux φ_m in the cavity. If we approximate φ_m by the product of the beam's unperturbed magnetic field at the cavity times the cavity cross-sectional area, we obtain the inductance[7]

$$L = \varphi_m / I = \frac{Z_0}{2\pi c} \frac{g\Delta}{a} \quad (\Delta/a \text{ small}) . \tag{10}$$

with I the beam current and Z_0 = 377 Ω. The inductance of a bellows-which is just a sequence of small cavities-can be approximated by the above result multiplied by the number of convolutions. Next we studied the shallow iris [see Fig. 4(c)]. The numerical results agree well with

$$L = \frac{Z_0}{\pi c} \frac{\Delta^2}{b} \quad (\Delta/b \text{ small, g/b small}) . \tag{11}$$

It appears that for the shallow iris the effective distance from the corner over which the magnetic flux changes with time is on the order of A.

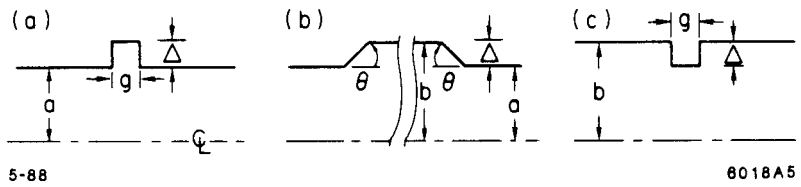

Fig. 4. Some simple vacuum chamber elements: (a) a small cavity, (b) a symmetric pair of shallow transitions, and (c) a shallow iris.

Finally we considered a pair of symmetric, shallow transitions [Fig. 4 (b)]. Our simulation results-if the transitions are separated by a distance at least on the order of b-can be approximated by

$$L = \frac{3Z_0}{2\pi c}\frac{a\Delta^2}{b^2}\left(\frac{2\theta}{\pi}\right)^{1/2} \qquad \text{(A/b small, } g/b \gtrsim 1,\ \theta \leq \pi/2) \quad . \tag{12}$$

Note that this equation approximates the numerical results well even for $\Delta/b \sim 0.5$. We see from Eq. (12) that when $\theta < \pi/2$ the inductance of a transition can be reduced, though only very slowly, by changing the transition angle. However, if we break up a transition into ***n*** smaller steps, that are separated by a sufficient distance, we can gain by the factor ***n.*** Note that Eq. (12) with $\theta = \pi/2$ must also apply to the iris of Fig. 4(c) when $g/b \gtrsim 1$.

For the example transition with parameters a = 10 mm and A/b = $1/6$ we demonstrate, in Fig. 5, the validity of the angular dependence of Eq. (12). The plotting symbols signify the computed results, the dotted curve the approximation Eq. (12). More specifically, the plotted values give the effective inductance ℓ computed for a 16 mm Gaussian bunch; when the bunch length was doubled the results remained essentially unchanged. We see that within its limits of validity Eq. (12) agrees very well with the computations. Note that, over the entire range of data points, the results of Fig. 5 vary roughly as $\sqrt{\tan(\theta/2)}$.

Finally we point out that the formulas of this section may also be used to estimate the imaginary part of the transverse impedance $Y_\perp$ at the origin for these

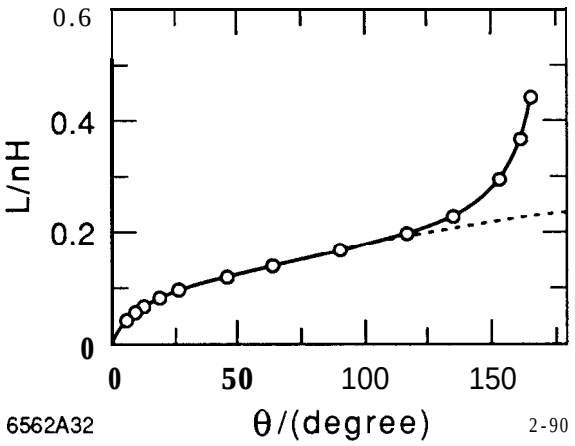

Fig. 5. The 6' dependence of **L** for a symmetric pair of shallow transitions when a = 10 mm and A/b = 1/6. The dotted curve gives the analytic approximation, Eq. (12).

structures. Using a well-known formula[8] for estimating the transverse from the longitudinal impedance of a cylindrically symmetric structure, with tube radius a, we find near the origin

$$Y_{\perp} \propto \frac{\mathcal{Z}}{a^2}\ell \quad . \tag{13}$$

2.5 The Damping Ring Vacuum Chamber

The damping ring vacuum chamber is divided into 8 girders (see Fig. 6). Of these girders 2, 3, 6 and 7 are almost identical. They each contain 4 1/2 FODO cells, with the quadrupole vacuum chambers-which are cylindrically symmetric—separated by the roughly square bend vacuum chambers (see Fig. 7). Girders 5 and 8, in addition to half a FODO cell on each end, contain kickers, septa, rf cavities and other vacuum chamber elements not found in the rest of the ring.

The vacuum chamber of the FODO cells can be divided into two groups of objects, each of which is repeated 20 times in the ring. One group, which we will call-a "QD vacuum chamber segment" is centered on a defocusing quadrupole vacuum chamber, with each end at the middle of the neighboring bend chamber.

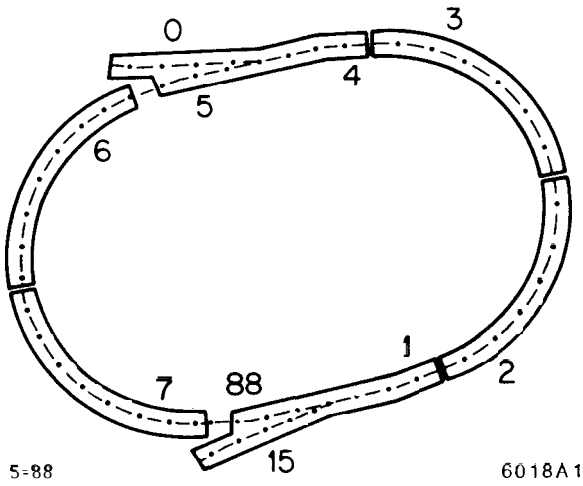

Fig. 6. The girders of the SLC north damping ring.

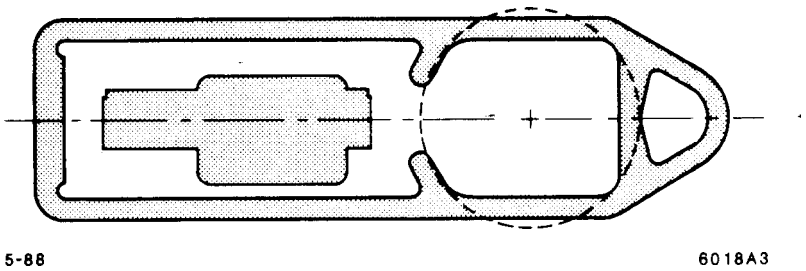

Fig. 7. The cross-section of the bend chamber. The dashed circle shows the size of a quad chamber.

The "QF vacuum chamber segment" is similar, though centered on a focusing quadrupole. The vertical profile of these segments is sketched in Fig. 8, with the ends truncated. Nonsymmetric portions are shown dashed. The figures are drawn to scale. The total length of each segment is about 60 cm; the half-length of the bend chamber is 15 cm.

A QD segment (see the top sketch) begins with the roughly square bend chamber (1), which is connected by a tapered transition (2) to the cylindrically symmetric defocusing quadrupole (QD) chamber. The QD chamber contains a 1 inch beam position monitor (1" BPM) (3), a QD bellows (4), a serf gasket (5), and a QD mask (6). Finally there is another transition (7) into the next bend (8). The

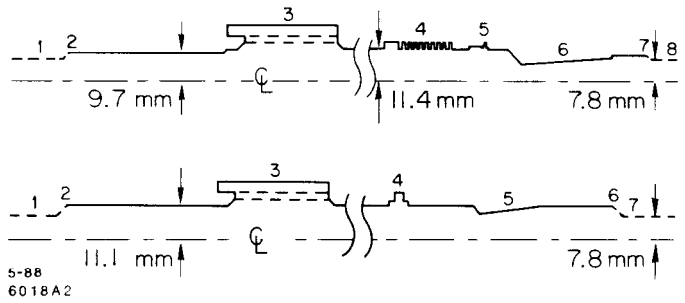

Fig. 8. The vertical profile of a QD segment (top) and a QF segment (bottom). The noncylindrically symmetric portions are drawn with dashes.

ends of a QF segment are similar (see the bottom of Fig. 8). The cylindrically symmetric QF chamber, however, contains a 1" BPM (3), a flex joint (4), and a QF mask (5).

Ring Girders 5 and 8 include two kickers, two septa, a two cell rf cavity, two 1" to 2" transitions, four 2" BPM's, four 1.4" BPM's, an optical monitor and a dielectric gap.

2.6 The Impedance of Individual Vacuum Chamber Elements

2.6.1 The Inductive Elements

In order to estimate the relative importance for bunch lengthening of the different objects found in the SLC damping rings we divided the vacuum chamber into a number of recognizable pieces. Then, for each piece we computed the wakefield of a Gaussian bunch with length σ = 6 mm using TBCI. This length was taken as typical for the damping rings. Then finally we obtained ℓ by performing a least squares fit, as described earlier. Note that dividing a stretch of several vacuum chamber objects into its parts does not affect the answer so long as $\sigma \gtrsim a/2$, with a the tube radius, and so long as neighboring pieces are separated by at least ***2a.*** With typically a = 11 mm the former condition is normally met. The latter condition, unfortunately, cannot always be met. Therefore, the results we present

only approximately give the relative importance of the various vacuum chamber objects.

Unfortunately, many of the vacuum chamber objects are not cylindrically symmetric. Whenever possible, we took a suitable cylindrically symmetric (2-D) model to represent the noncylindrically symmetric (3-D) object in the calculations. In some-cases it was evident how one might go about this. For example, the geometry of-the ion pump slots, a 3-D object, can partially be seen in Fig. 7. We see that each slot can be approximated by a simple, shallow transition, whose outer radius is defined by the pump housing, and which fills only 10% of the azimuth. For the slots, we computed the wakefield for a cylindrically symmetric version of the shallow transition using TBCI, and then multiplied the results by a filling factor of 0.1. The beam position monitors (BPM's), with their noncylindrically symmetric electrodes, were treated in a similar manner. In other cases, it was not so evident what the right 2-D model should be. For example, the QD and QF transitions are transitions from an approximately square to a round vacuum chamber tube. For such objects, we obtained insight into how best to model them by applying the computer program T3,[9] the 3-D counterpart of TBCI, to a simple 3-D approximation to the real structure.

Table 1 gives the results for the elements that are inductive to a 6 mm Gaussian bunch. Figure 9 shows the geometry used for (a) the QD bellows, (b) the QD mask, (c) the QD transitions, and (d) the ion pump slots. The factor in Column 3 is an azimuthal filling factor used to account for the contribution of noncylindrically symmetric objects. Column 4 gives the total number of these objects in the ring. We see that the total effective inductance of the ring is approximately 50 nH, spread over many objects. Not included in the table are the septa, each of which is a complicated obstruction in a 25 mm ID tube. Using the computer program T3 on a simple 3D model we find that the septum has an inductive and resistive component. We estimate that $\ell \approx 2$ nH for each septum.

Table 1. The inductive vacuum chamber elements.

Single Element Inductance		Contribution in Ring		
Type	L/(nH)	Factor	Number	L/(nH)
QD bellows	0.62	1.0	20	12.5
QD & QF masks	0.47	1.0	20	9.5
QD & QF trans.	0.52	0.9	20	9.3
Ion pump slots	1.32	0.1	40	5.3
Kicker bellows	2.03	1.0	2	4.1
Flex joint	0.18	1.0	20	3.6
1" BPM trans.	0.10	0.8	40	3.3
Other				2.4
		Total		50.0

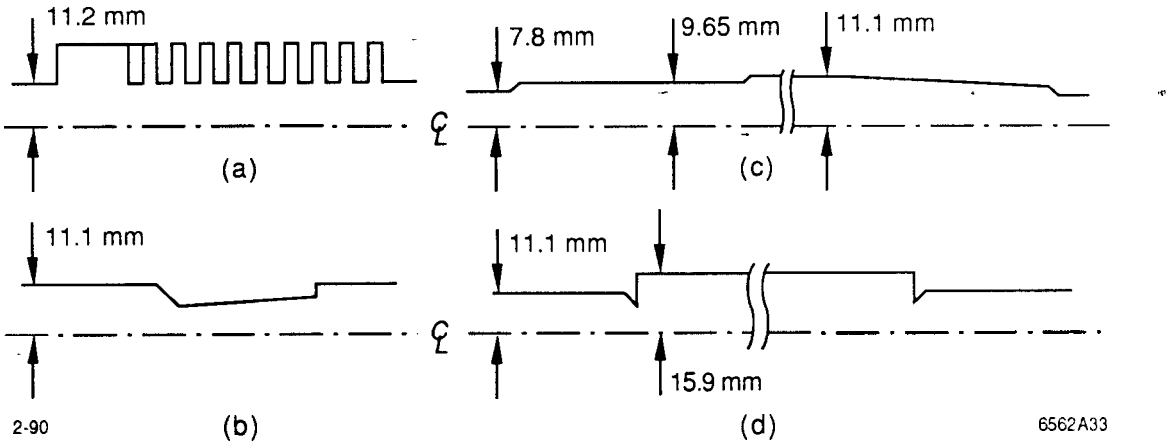

Fig. 9. The geometries used to calculate ℓ for: (a) the QD bellows, (b) the QD mask, (c) the QD transition, and (d) the pump slots.

Since the inductance of the ring is spread over so many objects it would take more than a small modification to reduce it significantly. Recently sleeves were installed to shield the QD bellows from the beam. From the table we would estimate that the ring inductance would therefore be reduced by 25%. However, since the bellows are close to the QD mask (see Fig. 8) there is coupling between these two objects. By performing the calculation for the entire QD segment taken

as one piece, once with and once without the bellows, we estimate the bellows contribution to the ring inductance to be more like 15%.

2.6.2 The Resistive Elements

There are objects in the ring that are resistive, most important of which are the two 2-cell rf cavities. At a bunch length of 6 mm the rf cavities contribute 5.8 V/pC to the-ring loss factor ***k.*** We can speak of them having an effective resistance of 411 Ω. At this bunch length the forty 1" BPM cavities are also resisitive with a total ***k*** of 3.2 V/pC. However, these small cavities become less resistive at longer bunch lengths. 0ther objects that are resistive at this bunch length, but contribute little to the ring loss are two 2" BPM's, two 1.4" BPM's, two kicker gaps, an optical monitor, the ion pump holes and a dielectric gap.

How can we compare the contribution of the inductive and the resistive vacuum chamber components to the longitudinal instability? In instability analysis the impedance enters as the quantity $|Z(n)/n|$, with-n = ω/ω_0 and ω_0 the revolution frequency. For the damping rings ω_0 = 5.4 x 10^7 s^{-1}. Therefore, for the inductive elements the effective inductance of 50 nH corresponds to an effective $|Z/n|$ of 2.6 Ω. For resistive elements let us consider only the rf cavities. If for the cavities we take as typical frequency w = l/o we find that an effective resistance of 411 Ω corresponds to an effective $|Z/n|$ of 0.44 Ω. According to this rough estimate the inductors contribute 6 times as much to the $|Z/n|$ of the ring as the cavities. If we want to bring the contribution of the inductors down to that of the rf cavities we would clearly need to rebuild the entire vacuum chamber.

2.7 The Green Function Computation

We will need a Green function wake for the damping rings in order to perform bunch length calculations. However, it suffices if we can find the wakefield of a bunch that is very short compared to the natural bunch length in the ring, and that has been calculated out to a sufficient distance behind the driving bunch. Ideally we would like to compute the wake for one whole turn around the ring in

one long computer run, with the beam moving from one element to the next just as it does in the real machine. Then all interference effects between neighboring elements, even at frequencies above cut-off, are properly accounted for. However, due to the limitations in computer time and memory available to us we need to make compromises.

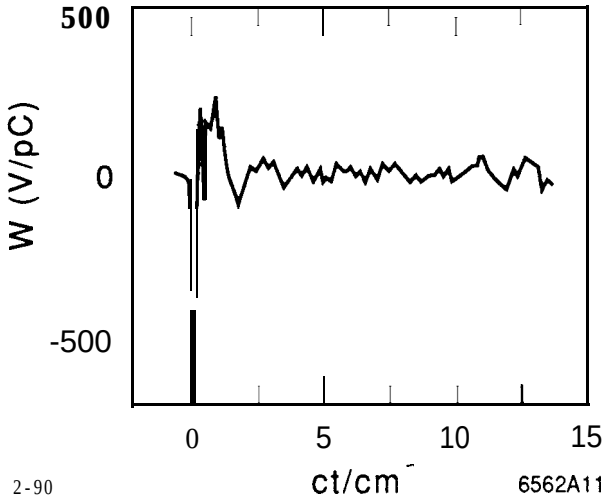

Fig. 10. The longitudinal wakefield of a 1 mm Gaussian bunch in the SLC damping ring.

For our Green function we first calculated the wakefield of a 1 mm Gaussian bunch, out to 15 cm behind the bunch, for the various damping ring vacuum chamber objects. The only exception is for the rf cavities, where a 2.7 mm bunch was used, due to limitations in the computer memory available to us. As best as possible we wanted to properly include the interference effects of neighboring objects. To this end we calculated the wakefields of the entire QD and QF segments each in one piece. To account for the noncylindrical symmetry of the BPM electrodes we performed the calculation for each segment twice--once with and once without cylindrically symmetric electrodes-and then added the two results in the ratio 8:2, according to the azimuthal filling factor of the real electrodes. However, the calculations of the pump slots, as well as of the remaining objects found in girders 5 and 8, were all done in separate computations. Objects that were not included

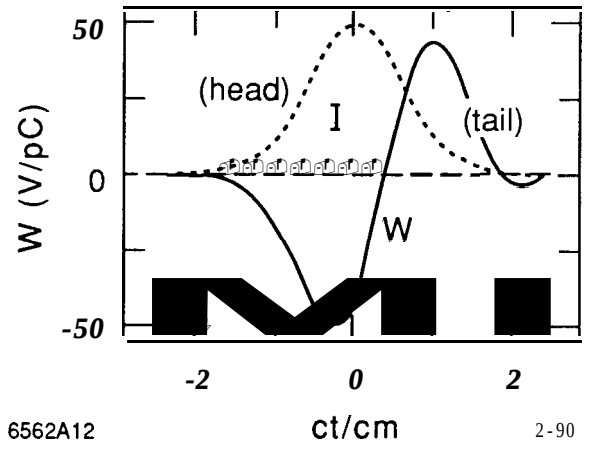

Fig. 11. The longitudinal wakefield of a 6 mm Gaussian bunch in the SLC damping ring. The current distribution is also shown.

in the calculations are the septa, the ion pump holes, the optical monitor, and the dielectric gap.

The sum of all the computations, which we take to represent the wakefield of a 1 mm Gaussian bunch in the SLC damping rings, is shown in Fig. 10. We note that most of the response occurs within the first 2 cm behind the driving bunch. By performing the integral of Eq. (9) we can find the wakefield of any Gaussian bunch that is longer than 1 mm. Figure 11 shows the results that are obtained for a 6 mm Gaussian bunch. At this length the ring is clearly very inductive.

In the same manner we have obtained the wakefields of Gaussian bunches with different lengths. From these wakefields we have found the loss factor k and the effective inductance ℓ of the ring as functions of bunch length. These results are shown in Fig. 12. The dotted curve gives the contribution to the loss factor of the rf cavities alone. We see that both k and ℓ reach asymptotic values at long bunch lengths. In addition, we see that the loss factor of the entire ring drops in an exponential fashion with increasing σ, while the loss of the rf cavities drops only very slowly.

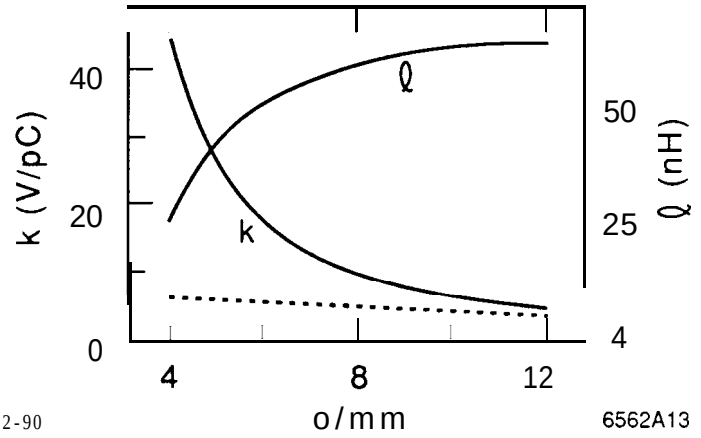

Fig. 12. The loss factor ***k*** and the effective inductance ℓ of the damping ring as function of bunch length. The dotted curve gives the loss contribution of the rf cavities alone.

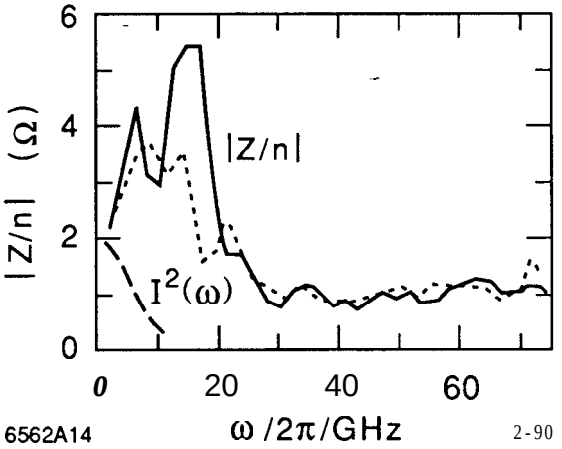

Fig. 13. The impedance $|Z/n|$ of the damping ring. The dots give what remains when the QD bellows (with their antechambers) are perfectly shielded. The power spectrum of a 6 mm Gaussian bunch is also shown.

By taking the Fast Fourier Transform of the 1 mm wake we can obtain the impedance. In Fig. 13 we plot the quantity $|Z/n|$ (remember ω_0 = 5.4 x 10^7 s^{-1}). We see a large broad peak at 16 GHz, with a peak value of 5.5 Ω and Q of 2; it is due mostly to the bellows. A smaller resonance, at 6.5 GHz, with a peak value 4.4 Ω, and a Q of about 1, is due to the BPM cavities. (We note, however, that the results

for this resonance may be very inaccurate, due to the very approximate manner in which we included the BPM electrodes.) In Fig. 13 we also see that $|Z/n|$ obtains a constant value at high frequencies, an effect that is due to numerical noise. When we repeat the calculation of the 1 mm wake, but this time leaving out the QD bellows, and then take the Fourier transform, we obtain the results shown by the dots in Fig. 13. These results are meant to represent the damping ring with the QD bellows shielded, as has recently been done. We note a substantial reduction in. the impedance beyond 10 GHz. Although we do not expect this modification to have a great effect on the bunch length it may still have a significant effect on the instability threshold.

From the 1 mm wake we contructed the Green function wake W_δ in the following manner: we first changed its sign and then modified the front of the function so that it is 0 for $t < 0$. This modification yields a Green function that is causal. This Green function will later be used to calculate the wakes for bunch shapes that are long compared to 1 mm and that are rather smooth. We therefore expect the results not to be very sensitive to the details of the modification just mentioned, provided that the changes are localized near $t = 0$ and that the area under the curve remains unchanged. For our calculations we have chosen to reflect the leading tail to the back, and then to add it to the existing wake. The leading part of the Green function wake is shown in Fig. 14. The dots give the negative of the 1 mm wake.

3. BUNCH LENGTHENING MEASUREMENTS

3.1 Introduction

Under normal SLC operations the beam, after leaving the damping ring, is shortened by about a factor of 10 in the Ring-to-Linac (RTL) transfer line before entering the linac proper. The bunch shortening is the result of a phase space rotation. It is accomplished by an rf section, which induces an energy variation that is correlated with longitudinal position, followed by a beam line with nonzero

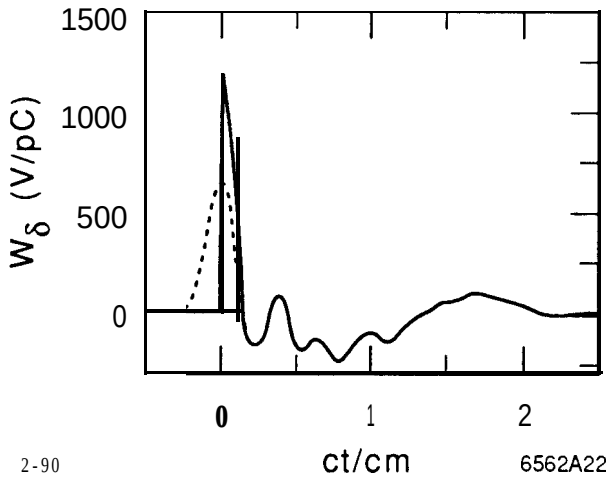

Fig. 14. The Green function wake for the SLC damping rings.

momentum compaction. Using this hardware and, in addition, a phosphor screen and video camera, we are able to measure the longitudinal charge distribution of individual damping ring pulses, of pulses having an rms length on the order of 5 mm. Although the measurements to be discussed contain some fluctuations due to screen imperfections, we expect that with a better, newly installed screen we can now measure the longitudinal intensity accurately to a resolution of 0.1 mm[10] for a bunch with a length of 5 to 10 mm.

Using the same hardware but with the compressor rf off, and with a modified optics, we can measure the bunch's energy distribution as function of current. In particular, this measurement allows us to find the threshold current for turbulence. We also discuss, in this chapter, measurements of the current dependence of the beam's synchronous phase and of the longitudinal quadrupole tune.

3.2 Measuring the Longitudinal Charge Distribution

3.2.1 ***Introduction***

The hardware, as it is configured for bunch length measurements, is shown in Fig. 15.. The setup is essentially the same as during normal operations. However, at a downstream position of high horizontal dispersion a phosphor screen is inserted in

the path of the beam. An off-axis camera can then capture the image, the intensity of which can-in turn-be digitized over a grid and sent to a computer. If we can assume that the response of the screen to charge intensity and the response of the camera to light intensity are linear, then the horizontal distribution measured in this way will be correlated to the longitudinal charge distribution in the ring.

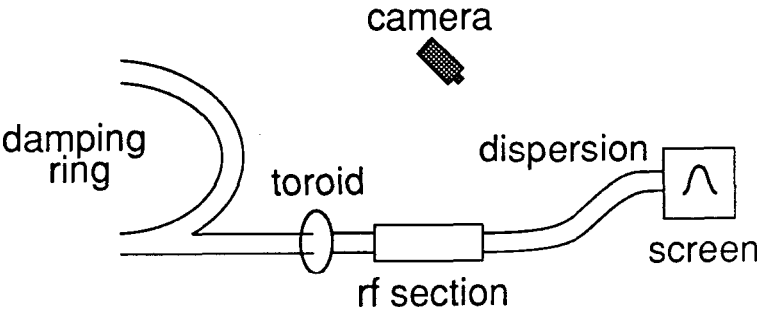

2-90 6562A1

Fig. 15. Layout of the apparatus used in the bunch length and energy spread measurements.

Now let us assume for the following discussion that (i) the longitudinal distribution does not reach past the crests of the rf wave, (ii) the induced energy spread is large compared to the beam's initial energy spread and compared to the wake-field induced energy variation, and (iii) the dispersive part of the beam size $(\eta^2\delta^2)$ dominates the emittance part $(\beta\epsilon)$. For the measurements about to be presented all these conditions were met. Given these assumptions, the connection between longitudinal position t within the bunch and transverse position x on the screen is

$$x - x_0 = \kappa \sin k_{rf}(ct - z_0) \quad , \tag{14}$$

with x_0 the screen position that corresponds to the zero of the rf the sine wave z_0, and k_{rf} the rf wave number. The parameter $\kappa = \eta e V_c/E$, with η the dispersion

at the screen, V, the peak compressor voltage, and E the beam energy. The longitudinal charge distribution is given by

$$\lambda = c\lambda_x \left|\frac{dx}{dz}\right| = c\lambda_x k_{rf}\sqrt{\kappa^2 - (x - x_0)^2} \quad . \tag{15}$$

Equations (14) and (15) allow us to obtain the beam distribution X(t) given the measured distribution $\lambda_x(x)$.

Note that in the SLC the compressor wave length is 10.5 cm and the beam energy E = 1.153 GeV. For the bunch length measurements we took $V_c \approx 33$ MV.

3.2.2 Results

We began the measurements by finding κ and x_0. Taking a low current beam we varied the rf phase and measured the excursion limits of the spot: the half distance between these two points gave us κ. Thus the dispersion and the compressor voltage do not need to be known explicit-ly. For our data κ = 18.25 mm; thus a 1 mm distance near x_0 on the screen corresponded to a 1.1 mm longitudinal distance within the bunch. Then measuring the spot with the compressor rf off gave us x_0. We then turned the compressor back on and adjusted the phase so the low current spot was again at x_0. With this setup we measured and stored the distributions over a range of currents, at a ring rf voltage V = 0.8 MV. For each measurement a toroid reading, giving us the current, was also taken.

As an example, Fig. 16 gives the measured distribution λ_x for a bunch population N = 2.9 x 10^{10} after it has been transformed to λ (as described above). The vertical axis is $y = eN\lambda Z_0/(\dot{V}_{rf}\sigma_0)$, with Z_0 = 377 Ω and σ_0 the natural bunch length ($c\sigma_0$ = 5 mm at this ring voltage); the horizontal axis is t/σ_0. We note that the distribution is broad and it is not symmetric: the rising edge is steeper than the falling edge. The corresponding centroid shift is a measure of the higher mode losses. For the moment, however, we should take the position t = 0 on the plot as arbitrary since the beam's position on the screen drifted over the duration of the measurements, apparently due to phase drift of the ring rf. (We will present

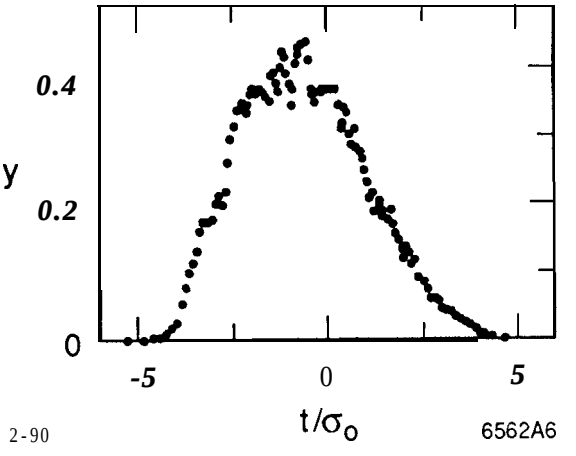

Fig. 16. The measured bunch shape for N = 2.9 x 10^{10} when V_{rf} = 0.8 MV.

more accurate measurements of the centroid shift below.) As in this example all the measured distributions are-quite smooth, except in the vicinity of their peaks. We believe the fluctuations that we do see in the-data are due to imperfections in the screen. Recently a new screen with a more uniform phosphor layer has been installed in the RTL. We expect, therefore, that future measurements will result in smoother distribution curves.

We present the rms widths of the distributions, times 2.355, as function of current in Fig. 17(c) (the full circles). On the same frame we plot the full-width-at-half-maximum (the open circles). For a Gaussian distribution these two quantities should be equal. That the open circles lie above the closed ones at higher currents implies that these distributions are more bulbous than a Gaussian. Note that there is very little scatter in the data.

We mentioned earlier that the current values of each measurement were based on toroid readings. However, we could alternatively have taken the areas under the distribution curves as the measure of current, since these areas are also proportional to the charge. In fact, with the areas one obtains a current reading for the same pulse that is being measured, whereas with the toroids one never knows to which pulse the reading corresponds. In any case, the pulse-to-pulse current variation

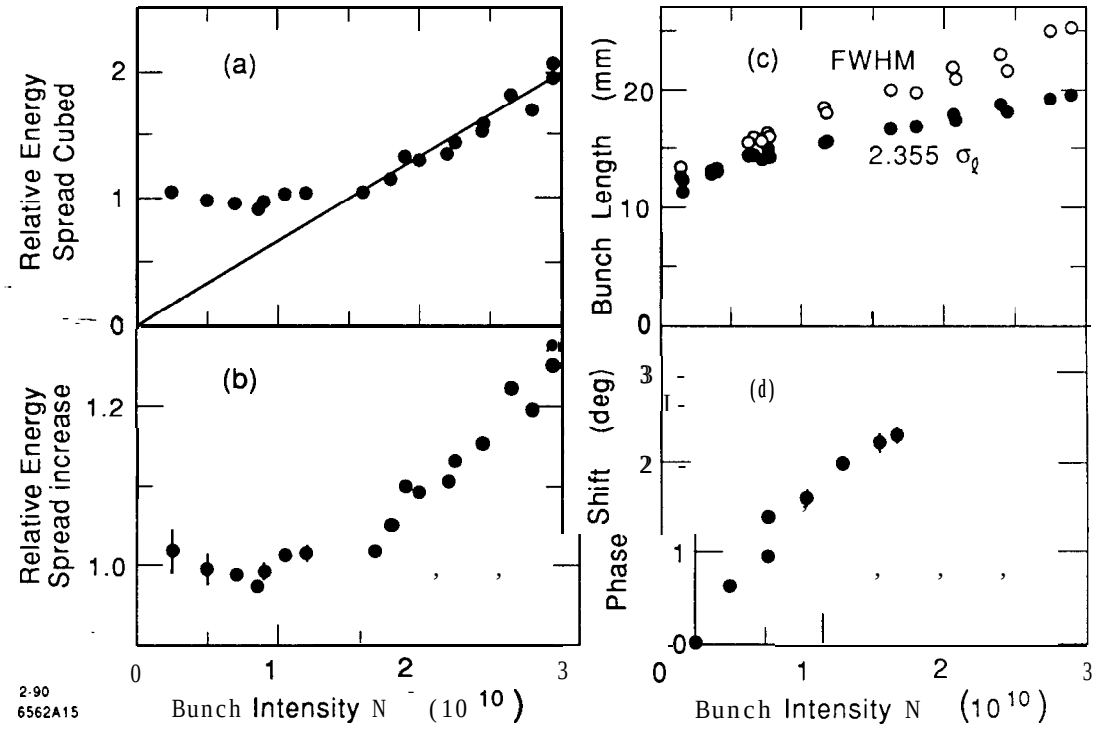

Fig. 17. Measurement results: (a) the relative energy spread cubed, (b) the relative rms energy spread, (c) the bunch length, and (d) the synchronous phase shift as function of current. The ring voltage V_{rf} = **0.8** MV.

was small during the course of our measurements. We found that the correlation of-the areas of the distributions with the toroid readings was extremely good. This suggests that, despite the local fluctuations that we saw in the distribution curves, the overall response of the hardware to intensity was essentially linear. When we plot the bunch length as function of distribution area rather than as function of toroid reading the data follows a smoother curve.

3.3 Other Measurements

3.3.1 Energy Spread Measurement

The beam's energy spread was measured in a fashion similar to its bunch length. For this measurement we turned off the compressor, used another screen, and modified the RTL optics to give an increased dispersion function at the screen.

In this configuration increases in the beam's intrinsic energy spread translate into an increased spot size on the screen. This measurement is difficult since at high currents the small, intense spot will tend to damage the screen.

The energy spread measurements yielded distributions that all appeared to be Gaussians. Figure 18 shows the measured distribution when N = 3 x 10^{10}, with a Gaussian curve superimposed on the data. The rms energy spread as function of current is displayed in Fig. 17(b). We see that the data is rather flat up to about N = 1.5 x 10^{10}, at which point it begins to rise. We will take this value as the threshold current N_{th}. By plotting the energy spread cubed as function of current [see Fig. 17(a)] we see that above threshold the data agrees well with

$$\sigma_\epsilon = \sigma_{\epsilon_0} \left(\frac{N}{N_{th}} \right)^{1/3} \qquad (N > N_{th}) \quad , \tag{16}$$

with σ_{ϵ_0} the initial energy spread. As we shall see in the next chapter, we expect the energy spread to behave in this way for a ring with an inductive impedance, such as the damping ring.

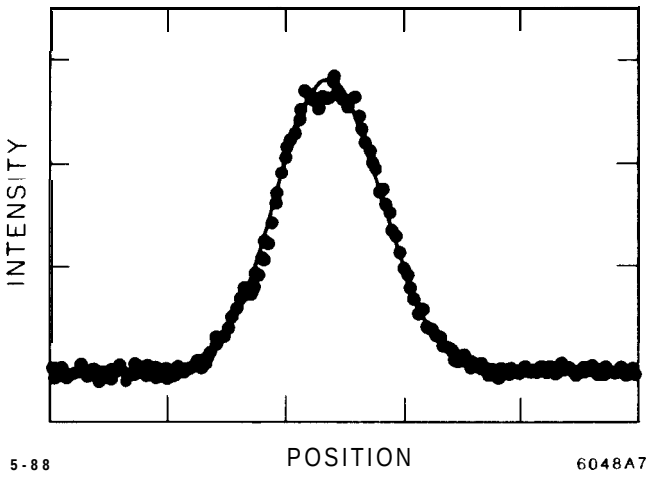

Fig. 18. The measured energy spectrum for N = 3 x 10^{10} when V_{rf} = 0.8 MV.

3.3.2 Measurement of the Synchronous Phase

The measurement of the synchronous phase complements the bunch length measurement. The bunch length measurement probes the imaginary part of the broad band impedance, while the synchronous phase measurement probes the real part, giving also the higher mode losses. We began the measurement by first storing a high current beam in the ring. Then, we gradually scraped away beam while we continually monitored the beam's phase using a vector voltmeter and a chart recorder. At the same time the circulating current, which we could continually read from a current monitor in the ring, was marked at frequent intervals on the chart. For more details of the measurement technique see Ref. (11).

The measured phase shift as function of current is shown in Fig. 17(d). The plot gives the average of several traces of the chart recorder, all of which agreed quite well with one another. The data grows linearly at low current, and more slowly as the current increases. This is the kind of behavior we would expect since, as we have seen above, as the damping ring current increases the bunch length also increases, and we know that the higher mode losses depend inversely on bunch length. Note that the total shift at N = 1.5 x 10^{10} is only 2.3 degrees. This size of shift corresponds to a higher mode loss of 32 keV and a loss factor k = 13 V/pC.

3.3.3 Synchrotron Tune Shift Measurement

Measuring the current dependence of the coherent oscillation frequencies is another way of probing the broad band impedance of the ring. Sometimes this coherent shift is also taken as a measure of the incoherent tune shift with current. In this measurement we excited quadrupole mode oscillations by amplitude modulating the rf gap voltage, and then measured the response from a beam position monitor. In Fig. 19 both the measured dipole and half the quadrupole frequencies are displayed over a range of currents. We see that the quadrupole frequency initially decreases but then appears to level off near N = 5 x 10^9. The maximum reduction is 3 to 4%. From the plot, we also see the dipole frequency, which should remain flat, rise slightly with current.

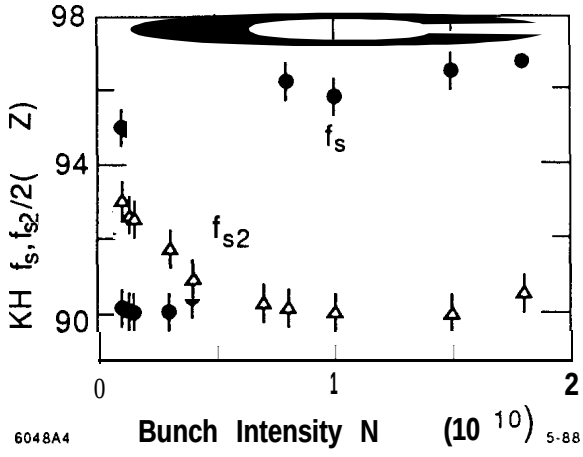

Fig. 19. The longitudinal dipole and half the quadrupole oscillation frequency as function of current.

3.4 Measurements Since the Addition of Bellows Sleeves

The bellows mentioned previously, in Chapter 2, are inner bellows; which are themselves surrounded by a set of outer bellows. Since the inner bellows are very inductive we normally expect a bunch to leave almost no energy behind after its passage. If, however, there is not a complete contact between the inner bellows and the vacuum chamber walls, then the beam can deposit energy in the cavity between the two bellows. We believe this to be the case for some of the QD bellows. During very high current operation it was observed that some of these bellows became very hot, in at least one instance resulting in a puncture of the outer bellows and a loss of vacuum. Largely to guard against more of this type of damage, and partly to reduce the bunch lengthening, sliding shields were placed within all the QD bellows in the North damping ring. This modification will be repeated in the South ring soon.

Since the introduction of the bellows shields in the North ring more bunch lengthening measurements were performed.[12] We found that the current dependence of the bunch length did not change significantly from the earlier measurements, at least up to currents of 2.8×10^{10}. We also repeated the energy spread

measurements. As mentioned before this measurement can be difficult. For currents greater than 1.5 x 10^{10} the beam, if left on the screen more than a moment, tended to damage it. Although we are not so confident in this new data, it appears that the turbulent threshold of the ring, at V_{rf} = 0.8 MV, has risen from 1.5 to about 1.9 x 10^{10} since the introduction of the bellows sleeves. We hope to repeat this measurement, and obtain better data, soon.

4. BUNCH LENGTHENING CALCULATIONS

4.1 Introduction

Once we know the Green function wake we can calculate the bunch shape as function of current. All our bunch length calculations are based on the theory of potential well distortion, as formulated by J. Haïssinski.[13] This method has been applied to a pillbox impedance,[14,15] to an rf cavity impedance,[16,17] and to a broad band resonator impedance,[18] to find-the steady state shape of a beam in a storage ring. Given the potential well, we can also calculate the amplitude dependence of the tune within the well. E. Keil has performed this calculation for a pillbox impedance.[15]

We begin this chapter by reviewing potential well theory and describing the calculation of the incoherent tune. We follow by describing our method for extending the calculations into the turbulent regime. Then, in order to illustrate different types of behavior, we give the bunch shapes and the tune distributions for a purely inductive, resistive, and capacitive impedance. Finally, we repeat the calculations using the Green function for the damping rings, and compare the results with the measurements.

4.2 Potential Well Distortion[13]

The steady-state phase space distribution in a storage ring $\psi(\epsilon, t)$ is given by the Hamiltonian of the system ***H:***

$$\psi(\epsilon, t) = e^{-H(\epsilon,t)} \quad . \tag{17}$$

For electron machines below the threshold current for turbulence the Hamiltonian is-up to an arbitrary constant-given by

$$H(\epsilon, t) = -\frac{\epsilon^2}{2\sigma_\epsilon^2} - \frac{t^2}{2\sigma_0^2} + \frac{1}{\dot{V}_{rf}\sigma_0^2}\int_0^t V_{ind}(t')\,dt' \quad , \tag{18}$$

with-s, the energy spread, σ_0 the natural bunch length, $\dot{V}_{rf}$ the slope of the rf voltage at the position of the bunch (we assume the applied rf wave is linear) and V_{ind} the transient induced voltage. In Eq. (18) a smaller value of t signifies an earlier point in time, while t = 0 designates the synchronous point for a low current beam.

The induced voltage V_{ind} is given by

$$V_{ind}(t) = -\int_0^\infty W_\delta(t')I(t - t')\,dt' = -\int_0^\infty S(t')\dot{I}(t - t')\,dt' \quad , \tag{19}$$

with $W_\delta(t)$ the longitudinal Green function wakefield, I the current [note: $I = eN\lambda$], and S(t)-known as the step function response--the indefinite integral of $W_\delta(t)$. By taking the phase space distribution and integrating out the energy dependence we find the longitudinal charge distribution. Then, by multiplying by the total charge Q [Q = eN] we obtain the current:

$$\mathrm{I(t)} = K\exp\left(-\frac{t^2}{2\sigma_0^2} + \frac{1}{\dot{V}_{rf}\sigma_0^2}\int_0^\infty S(t')I(t - t')\,dt'\right) \quad , \tag{20}$$

with K a normalization constant. Note that $I(t)$, the unknown, is on both sides of Eq. (20). However, note also that at time t the integral on the right depends only on the current at more negative (earlier) times. Therefore, we can solve for $I(t)$ numerically by beginning far in front of the beam (say at $t = -5\sigma_0$), where we assume the induced voltage is zero, and then proceeding, in small time steps, to the back of the bunch. And then finally, if the area under the newly computed

curve does not equal Q we adjust K, and iterate the whole procedure until it does. Taking the derivative of both sides of Eq. (20) yields an alternative form of it:

$$\frac{\dot{I}}{I} = -\frac{t}{\sigma_0^2} + \frac{V_{ind}}{\dot{V}_{rf}\sigma_0^2} \quad . \tag{21}$$

This form of the problem is more convenient when V_{ind} is given explicitly in terms of I, as is the case for the simple inductive, resistive, and capacitive models that we consider later. Of particular interest to us will be the rms length, the full-width-at-half-maximum, and the centroid shift of the current distribution. The ratio of the first two quantities is a measure of the similarity of the distribution to a Gaussian. Due to energy conservation the third quantity, when multiplied by $-\dot{V}_{rf}$, gives the higher mode losses.

In what follows all distances will be given in terms of σ_0. Thus the independent variable becomes x = t/σ_0. We will also normalize voltages to $\dot{V}_{rf}\sigma_0$: the induced voltage becomes $v_{ind} = V_{ind}/(\dot{V}_{rf}\,\sigma_0)$, and the total voltage v = $v_{ind} - x$.

4.3 The Incoherent Synchrotron Tune

Once we know the current shape, we also know the shape of the potential well. For convenience let us choose the bottom of the well to be at zero energy. Then the potential energy is simply given by $u = -\ln(I/\hat{I})$ with $\hat{I}$ the peak of the distribution. Given the shape of the potential well we can numerically solve for the incoherent synchrotron tune.

The equation of motion for a test particle moving in the well is

$$\frac{d^2x}{d\tau^2} - 4\pi^2 v(x) = 0 \quad , \tag{22}$$

with τ the time in units of the low current synchrotron period and v the total voltage. If the test particle has the initial conditions x = $\hat{x}$ and x' = 0 then its period of oscillation is given by

$$\mathcal{T} = \frac{1}{\sqrt{2}\pi}\int_{\hat{x}}^{x_c} \frac{dx'}{\sqrt{u(\hat{x}) - u(x')}} \quad . \tag{23}$$

The integration is performed over half a cycle: beginning at $\hat{x}$, we move down the potential well and up the other side until we reach the position x_c for which $u(x_c) = u(\hat{x})$. Note that when $v_{ind} = 0$ $[u(x) = x^2/2]$ then $\mathcal{T} = 1$. The relative incoherent tune ν is simply given by $1/\mathcal{T}$. Note that from Eq. (23) we can find the tune either as function of $\hat{x}$ or as function of energy $h = u(\hat{x})$.

If we know the tune as function of h, then we can also calculate the tune distribution:

$$\lambda_\nu = \sum_{h(\nu)} \frac{\lambda_h}{|d\nu/dh|} = \sum_{h(\nu)} \frac{e^{-h}}{|d\nu/dh|} \quad . \tag{24}$$

The sum in Eq. (24) is there to indicate that if more than one value of h corresponds to a certain value of ν we need to sum the contribution from each correspondence. This w-ill happen when there is an interior extremum of v(h). It will also happen when v(h) has more than one branch, as will occur when there is a relative maximum in the potential well curve. Note also that Eq. (24) implies that wherever $d\nu/dh = 0$ the distribution is infinite.

4.4 Some Simple Impedance Models

Over a frequency interval the impedance of vacuum chamber elements can often be characterized by a simple electrical circuit element-an inductor, a resistor, or a capacitor. We study in this section the potential well distortion when the whole ring can be characterized by these simple models.

4.4.1 An Inductive Impedance

For a purely inductive impedance the induced voltage is given by $V_{ind} = -L\, dI/dt$, with the constant L the inductance. Bunch lengthening has been observed in many storage rings, and we expect it to be due to an inductive impedance. In the case of the SLC damping rings we have seen that the impedance is dominated by the many inductive vacuum chamber elements. We, therefore, expect the general features of the bunch shape to be given by this model. Note that Haïssinski has presented numerically calculated bunch shapes for this model in Ref. (13).

For a purely inductive impedance Eq. (21) can be written as

$$y' = -\frac{xy}{1+y} \quad , \tag{25}$$

with prime denoting the derivative with respect to x = t/σ_0. The normalized current is given by y = $LI/(\dot{V}\sigma_0^2)$; the normalized charge I'(the complete integral of y) equals $LQ/(\dot{V}\sigma_0^3)$. The normalized induced voltage $v_{ind} \equiv V_{ind}/(\dot{V}_{rf}\sigma_0) = -y'$.

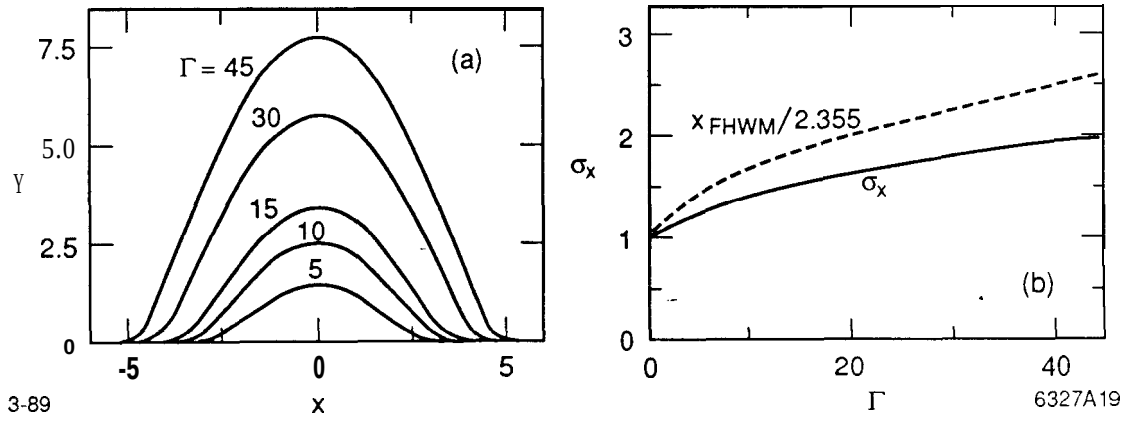

Fig. 20. An inductive impedance: (a) the bunch shape for several values of bunch population and (b) the bunch length variation as a function of current.

The numerical solution of Eq. (25), for several values of Γ, is shown in Fig. 20(a). Note that the charge distribution for a perfect inductor is symmetric about x = 0 (since there are no losses) and is more bulbous than a Gaussian distribution. From Eq. (25) it is apparent that the solution is parabolic wherever y >> 1. In Fig. 20(b) we display σ_x and $x_{FWHM}/2.355$ (the dashes) as functions of Γ. Note that for large currents σ_x varies roughly as $I^{1/3}$. If we apply the inductive model to the SLC damping rings, taking L = 50 nH, then an intensity of Γ = 7.5 corresponds to N = 1.5 x 10^{10} at V_{rf} = 0.8 MV. At this current we see from Fig. 20(b) that σ_x = 1.33 and x_{FWHM} = 3.69. We shall see, in a future section, that these values

approximate the results of the more detailed calculations, calculations that use the Green function wake.

Consider a current of Γ = 7.5 in an inductive machine. Now suppose a test particle is initially at rest at position x = $\hat{x}$ in the potential well. Figure 21(b) then displays the tune ν as function of $\hat{x}$. Only half of the curve is shown; since the well is symmetric about the origin $\nu(\hat{x}) = \nu(-\hat{x})$. We see that the tune decreases monotonically as $\hat{x}$ approaches zero, and that it. is very much depressed at the bottom of the well, to about 60% of its nominal value. On the same plot ν as function of energy $h = u(\hat{x})$ is also shown. We note that the slope of the tune is nonzero for h = 0, i.e., at the bottom of the well. In Fig. 21(a) we give the tune distribution λ_ν. [It is plotted sideways so that its connection with $\nu(\hat{x})$ and $\nu(h)$ is easier to see.] We note that the peak of the distribution is at the tune minimum, that the tune at the peak is greatly depressed, and that the distribution is broad.

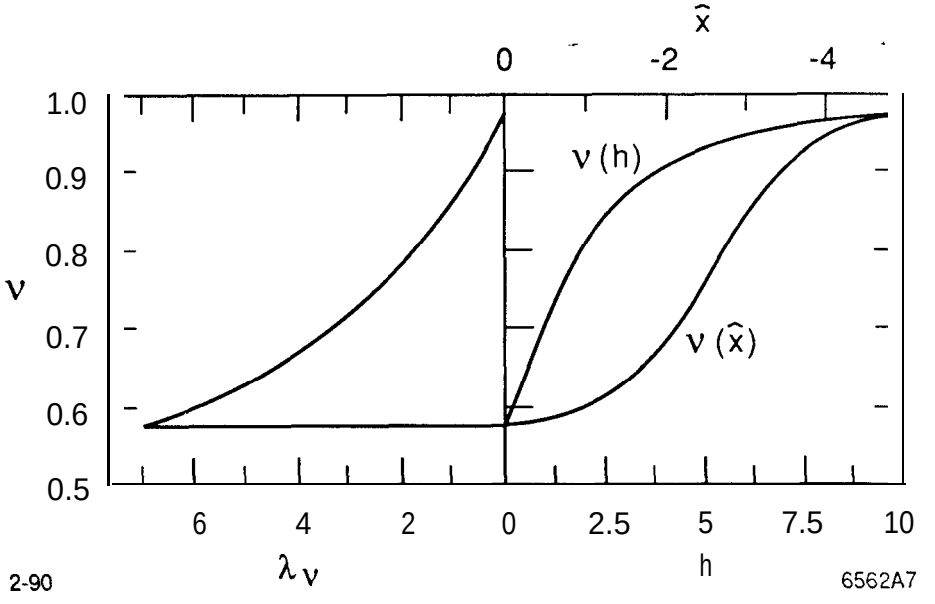

Fig. 21. (a) The tune distribution and (b) the dependence of tune on $\hat{x}$ and h when I'= 7.5 for an inductive impedance.

Let us use the following notation: let ν_x denote the tune above the fraction of the beam given by x. Thus $\nu_{.50}$ gives the median value of the tune. Then Fig. 22

displays as functions of current the tune at the peak of the tune distribution ν_0, as well as $\nu_{.25}$, $\nu_{.50}$, $\nu_{.75}$, and $\nu_{.95}$. We see that ν_0 drops most quickly at the low end of the current scale, and levels off at the high end. Note that for $\Gamma > 0.5$ the curve for ν_0 in Fig. **22** can be approximated by $1-0.15(1+\ln \Gamma)$. We can estimate the low amplitude tune shift $\Delta\nu_0$ at low currents by assuming the bunch remains Gaussian and that -y"(O) is small compared to 1. Then $\Delta\nu_0 \approx$ y"(O)/2 $\approx -\Gamma/(2\sqrt{2\pi}) \approx -0.2\Gamma$. -The quantity $1-0.2\Gamma$ is given by the dotted curve in Fig. 22. We note that it only approximates ν_0 for very low currents. At Γ = 0.5 it already deviates from the exact calculation by 30%. For the damping ring this current corresponds to a bunch population of only 10^9.

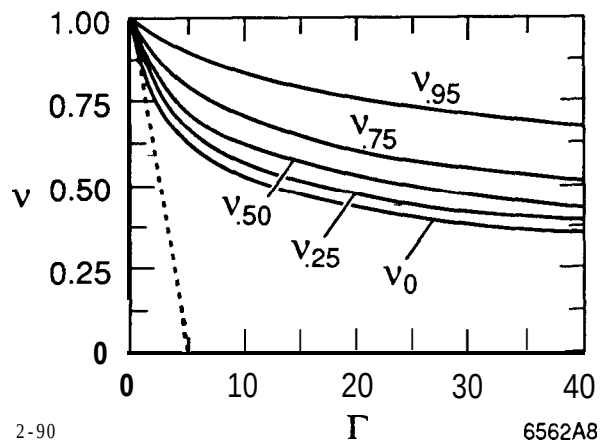

Fig. 22. The current dependence of the characterizing parameters of the tune distribution ν_0, $\nu_{.25}$, $\nu_{.50}$, v.75, and $\nu_{.95}$, for an inductive impedance.

4.4.2 A Resistive Impedance

For an ideal resistive impedance the induced voltage can be written as $V_{ind} = -IR$, with the constant ***R*** the resistance. This model is applicable to electron rings that don't have many inductive elements, and whose impedance is dominated by the rf and other large cavities. In storage rings where the builders have been very careful to avoid transitions and bellows we would expect the impedance to be resistive.

For an ideal resistive impedance Eq. (21) becomes

$$y' = -(x + y)y \quad , \tag{26}$$

with y = $RI/(\dot{V}\sigma_0)$ and $\Gamma = RQ/(\dot{V}\sigma_0^2)$. Note that $v_{ind} = -y$. The analytic solution to Eq. (26) was found by A. Ruggiero[19]:

$$y = \sqrt{\frac{2}{\pi}} \frac{e^{-x^2/2}}{\coth(\Gamma/2) + \operatorname{erf}(x/\sqrt{2})} \ , \tag{27}$$

with $\operatorname{erf}(x)$ the error function.

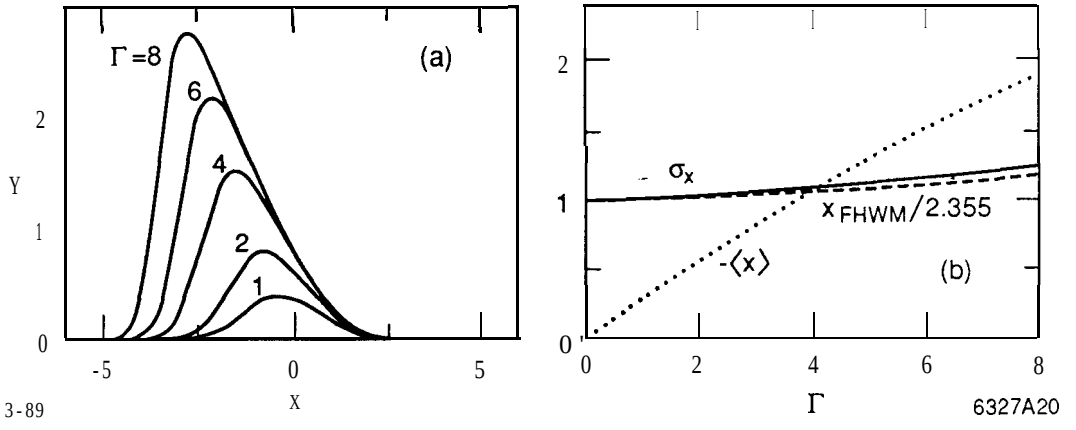

Fig. 23. A resistive impedance: (a) the bunch shape for several values of total charge and (b) the change of bunch length and centroid position (dots) with current.

The solution, Eq. (27), for several values of current is displayed in Fig. 23(a). As Γ is increased the bunch tilts forward (up the rf wave) by an ever increasing amount, in order to compensate for the increased higher mode losses. Figure 23(b) gives σ_x and $x_{FWHM}/2.355$ (the dashes). We see that the bunch length increases only very slowly in a resistive machine. The dots give the centroid shift (x) of the bunch. It can be approximated by $\langle x \rangle = -\Gamma/(2\sqrt{\pi})$, which is the centroid shift assuming that the bunch shape does not change with I.

Suppose we could remove all the impedance of the SLC damping rings except that of the rf cavities. As we saw before, we could approximate what was left by a resistive impedance with R = **411** Ω. A bunch population of 5 x 10^{10} in this ideal machine, when V_{rf} = 0.8 MV, corresponds to I'= 3.4. For this current Fig. 24(b) displays the tune as function of the maximum extent of oscillation $\hat{x}$, for $\hat{x}$ more negative than the position of the bottom of the potential well. We see that for both low and very high amplitude oscillations the tune is not changed. For amplitudes in between these two extremes, however, the tune is depressed, but by a very small amount. Also shown on the plot is the tune as function of energy v(h).

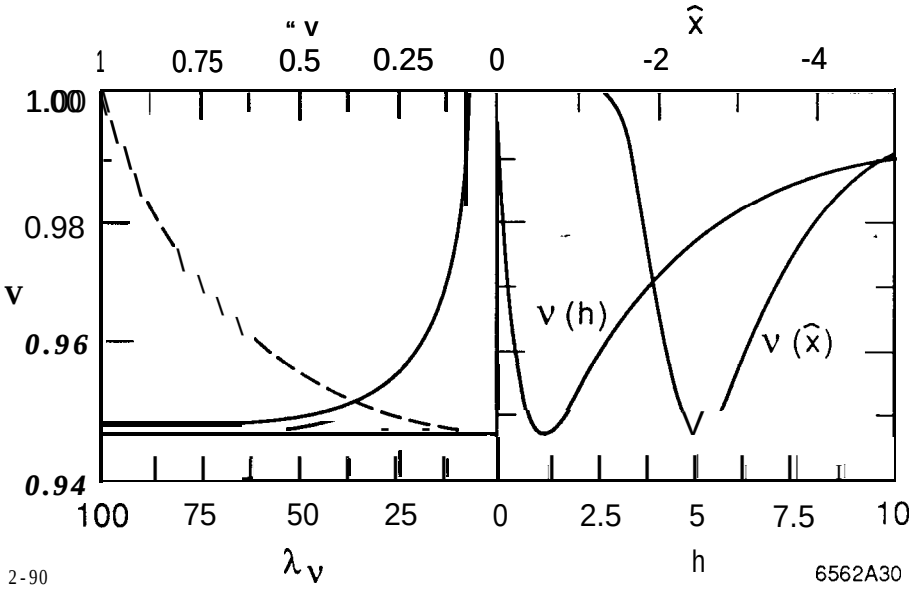

Fig. 24. (a) The tune distribution and its integral (dashes) and (b) the dependence of tune on $\hat{x}$ and h when I'= 3.4 for a resistive impedance.

In Fig. 24(a)we show the tune distribution λ_ν. Note that there is an infinite spike at the lowest tune value. The dashed curve in the figure gives the integral of the tune distribution n_ν. We note that 50% of the particles have tunes in the lowest 20% of the tune range. In Fig. 25 we give as function of current the parameter ν_0, $\nu_{.25}$, $\nu_{.50}$, $\nu_{.75}$, and $\nu_{.95}$ that charactrize the tune distribution.

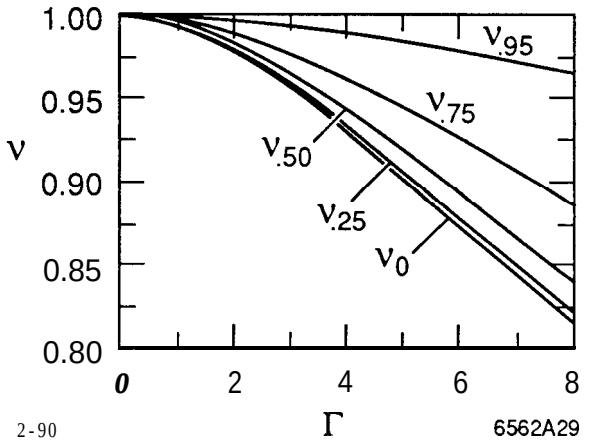

Fig. 25. The current dependence of ν_0, $\nu_{.25}$, $\nu_{.50}$, $\nu_{.75}$, and $\nu_{.95}$ for a resistive impedance.

4.4.3 *A Capacitive Impedance*

For an ideal capacitive impedance the induced voltage is proportional to the integral of the current, with constant of proportionality -l/C, and C the capacitance. Deep cavities, such as the rf cavities, are slightly capacitive at normal bunch lengths, and become more capacitive for very short bunches. Of the three simple models the capacitive is probably the least applicable to the types of impedances one finds in storage rings. We note that bunch shortening has not been observed in storage rings, except possibly at low currents in SPEAR, when the ring had many rf cavities.[20]

For a purely capacitive impedance Eq. (21) becomes

$$y' = -y[x + \int_{-\infty}^{x} \mathrm{Y}(x')dx'] \quad , \tag{28}$$

with y = $I/(\dot{V}_{rf}C)$ and $\Gamma = Q/(\dot{V}_{rf}\sigma_0 C)$. The solution to Eq. (28) closely approximates a Gaussian that has been shortened and shifted. Since the energy stored in a capacitor is $Q^2/2C$, the centroid shift is given by $\langle x \rangle = -\Gamma/2$. Figure 26 shows the bunch length dependence on I'. By substituting a Gaussian into Eq. (28) we

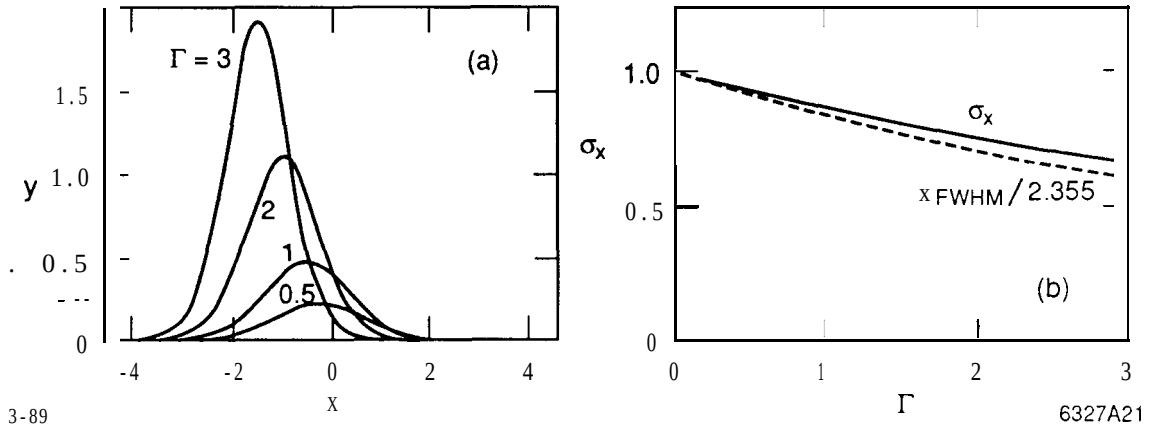

Fig. 26. (a) The bunch shape for various currents and (b) bunch shortening as a function of current, for a capacitive impedance.

can arrive at an analytical approximation of the bunch shortening, which for small current becomes $\sigma_x \approx 1 - \Gamma/\sqrt{8\pi}$.

In a capacitive machine the bunch becomes shorter and the tune of all the particles will rise. As was the case for the inductive machine the tune as function of energy is monotonic. The low amplitude particles have the highest tune. Their tune shift can be approximated by $\Delta\nu \approx 1/\sigma_x \approx \Gamma/\sqrt{8\pi} \approx 0.2\Gamma$.

4.5 The Turbulent Regime

4.5.1 ***Calculations Beyond Threshold***

Beyond some threshold current the energy spread begins to increase, and we enter what is known as the turbulent regime. At the moment, there is, unfortunately, still no reliable calculation of the behavior of short bunches in this regime. However, for a formalism that at least in theory can be used to solve the problem see, for example, J. M. Wang and C. Pellegrini.[21]

In the case of SLC damping rings, however, we will use a simpler method. We believe that the instability that we find in the damping rings is a fast instability of the microwave type, and we expect the potential well approach to calculating the bunch shape still to be applicable. As threshold current we take the value

given by the measurements. To find the bunch shape beyond this current we (i) scale the energy spread according to the Boussard criterion (see below), and then (ii) perform the normal potential well calculation but replacing σ_0 in Eq. (20) by $\sigma_0' = \sigma_0\sigma_\epsilon/\sigma_{\epsilon_0}$, with σ_{ϵ_0} the nominal energy spread. Implicit in our method is the assumption that the energy distribution remains Gaussian.

4.5.2 The Boussard Criterion

The Boussard criterion is often used to estimate the threshold for instability. Boussard[22] conjectured that the longitudinal instability in a bunched beam is due to a coasting-beam-like instability within the bunch. Then in estimating the threshold for instability one might use the coasting beam threshold[23] but replacing I by $\hat{I}$ the peak current. The issue of the applicability of a coasting beam instability criterion to a bunched beam was studied in detail by J. M. Wang and C. Pellegrini.[21] They found that one obtains a coasting-beam-like instability condition provided that: (i) the impedance is broad band relative to the bunch spectrum, (ii) the growth rate is much greater than the synchrotron frequency, and (iii) the instability occurs at wavelengths much shorter than the bunch length.

Their threshold condition looks like a coasting beam threshold condition[21]:

$$\frac{e\hat{I}|Z(n)/n|}{2\pi\alpha E\sigma_\epsilon^2} \leq 1 \quad , \tag{29}$$

with Z the broad band (or smoothed) impedance and n = ω_1/ω_0 , with ω_1 a representative frequency sampled by the bunch spectrum and ω_0 the revolution frequency; with α the momentum compaction factor and E the beam energy. Equation (29) is a stability condition, i.e., a condition for no fast blow-up. In our calculations we will take as threshold the measured value, and use Eq. (29) solely for scaling the energy spread in the turbulent regime.

In Eq. (29) both $\hat{I}$ and Z/n in general depend on bunch length which, in turn, depends on the energy spread. Consider, for example, a very resistive impedance where $Z = R$ the resistance. As typical frequency $n\omega_0$ we might take the inverse

bunch length. Then since $\hat{I}$ is also proportional to the inverse bunch length we find that Eq. (29) implies that, above turbulence, $\sigma_\epsilon \sim N^{1/2}$, with N the bunch population, for a resistive machine. On the other hand, for a very inductive machine, such as the SLC damping rings, $|Z/n|$ is approximately constant. If we substitute the peak current for a Gaussian beam in Eq. (29), and note that the bunch length is proportional to the energy spread, we see that, above threshold,

$$\sigma_\epsilon = \sigma_{\epsilon_0} \left(\frac{N}{N_{th}} \right)^{1/3} \qquad (N > N_{th}) \ , \tag{30}$$

with N_{th} the threshold current. This is the scaling we will use for calculating the damping ring bunch shapes in the turbulent regime.

We make two observations: (1) This scaling is roughly supported by the measurement results discussed in Chapter 3. (2) For an inductive machine the bunch length increases with current due to potential well distortion, and thus the growth of the peak current with current is somewhat reduced. To be more consistent we could have included this fact in determining the scaling of energy spread with current. For the purely inductive impedance discussed earlier we find that the peak current increases approximately as $N^{0.8}$, rather than as simply N, due to potential well distortion. Thus, for the damping rings we would expect σ_ϵ to vary as $N^{0.27}$ rather than as $N^{1/3}$ above threshold. And this modification, in turn, would result in a slight reduction in the calculated bunch lengths at the higher currents. For the results to be presented, however, the difference would not be significant.

4.5.3 Another Threshold Criterion

P. B. Wilson[24] has suggested that one threshold criterion might be that the slope of the total voltage v'becomes zero (or equivalently $u'' = 0$) somewhere within the bunch. This criterion has also been studied by G. Besnier,[18] who has used it to predict turbulent bunch lengthening for ESRF, the European light source. It is easy to show that if we assume a purely inductive impedance, and we also assume that the bunch shape remains Gaussian, then Wilson's criterion is equivalent to

the Boussard criterion. We can also show that this condition can never be met for the models of a purely inductive, resistive, or capacitive impedance. For it to be met requires some high frequency structure in the impedance curve (as is the case, for example, for the broad band resonator model with a high frequency resonance). Note that if Wilson's conjecture ($u'' = 0$) is met at the bottom of the potential well, then the tune becomes zero for small amplitudes. If, however, u" = 0 is first met at another position within the bunch, as we will see in our potential well calculations using the damping ring Green function, then the physical significance of the conjecture is not so clear.

Wilson's conjecture suggests another, more stringent threshold condition with a simple physical interpretation. Consider as threshold criterion that there be a relative maximum in the potential well shape, i.e., u' = 0, $u'' < 0$, somewhere within the bunch. If this condition is met then there will be two stable fixed points within the bunch and one unstable fixed point at the position of the maximum. Consequently, a subset of bunch particles will oscillate about a relative minimum of the potential well, rather than about the absolute minimum. Note that this is a more stringent condition than Wilson's and will tend to be met at higher currents than his condition. Finally, we should stress that both these threshold criteria are merely conjectures. Their validities need to be demonstrated in a self consistent manner.

4.6 Bunch Lengthening in the SLC Damping Rings

4.6.1 The Bunch Shape

Using our pseudo-Green function (see Fig. 14) in the potential well equation, Eq. (20), we have calculated bunch shapes for many values of current, for a ring voltage V_{rf} = 0.8 MV. Figure 27(a) displays the rms length σ_x and $x_{FWHM}/2.355$, and Fig. 27(b) gives the centroid shift (x) of the calculated distributions as functions of current. Length dimensions are again given in units of σ_0 (at this rf voltage $c\sigma_0$ = 4.95 mm). In Chapter 3 we saw that the measured threshold at this rf voltage was $N_{th} = 1.5 \times 10^{10}$. Taking this as our threshold, we extended the po-

tential well calculations into the turbulent regime by simply scaling the parameter σ_0 as $(N/N_{th})^{1/3}$, as was discussed earlier. (The turbulent regime is indicated by the dashed lines in the figure.) Superimposed on the curves are the measurement results presented in Chapter 3.

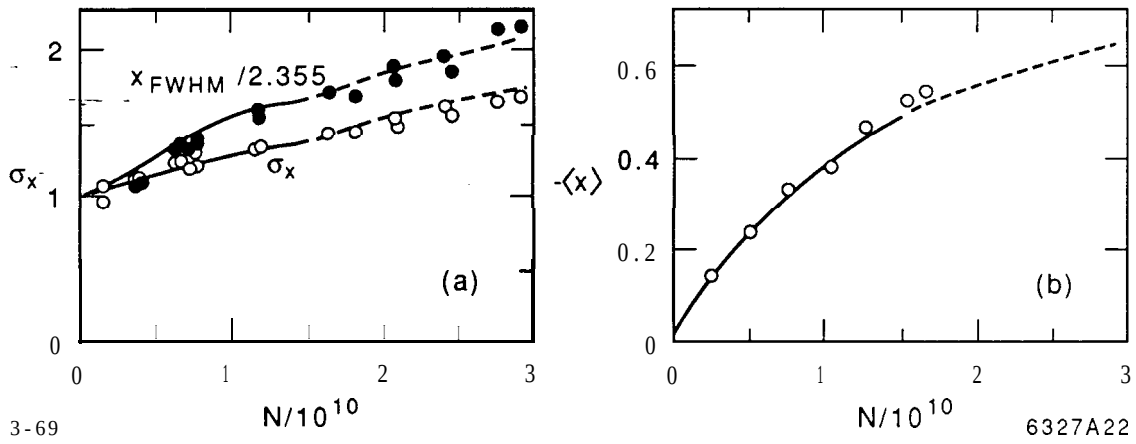

Fig. 27. (a) Bunch lengthening and (b) the centroid shift calculated for the SLC damping rings at V_{rf} = 0.8 MV. The symbols indicate the measurement results.

As we saw for the simple inductive model the current distributions calculated for the damping rings are more bulbous than a Gaussian. At N = 1.5 x 10^{10}, we see that σ_x = 1.38 and and x_{FWHM} = 3.93. These values compare well with those obtained assuming a purely inductive machine with L = 50 nH, for which we found σ_x = 1.33 and and x_{FWHM} = 3.69. The turbulent threshold is seen as a slight kink in the curves. Beyond this point σ_x varies roughly as $N^{1/3}$. We see that at N = 3 x 10^{10} the rms bunch length is increased by 70%. From Fig. 27(b) we see that the calculations give a significant amount of higher mode losses. At N = 1.5 x 10^{10} the centroid shift $\langle x \rangle$ = -0.5 is equivalent to a higher mode loss of 30 keV; at 3 x 10^{10} the loss is 38 keV. For both the bunch length and the centroid shift the calculations agree well with the measurements.

In Fig. 28 we present the bunch shapes for bunch populations of N = 0.7, 1.2, 2.1, and 2.9 x 10^{10}. The abscissas give x = t/σ_0, the ordinates are $y = IZ_0/(\dot{V}\sigma_0)$

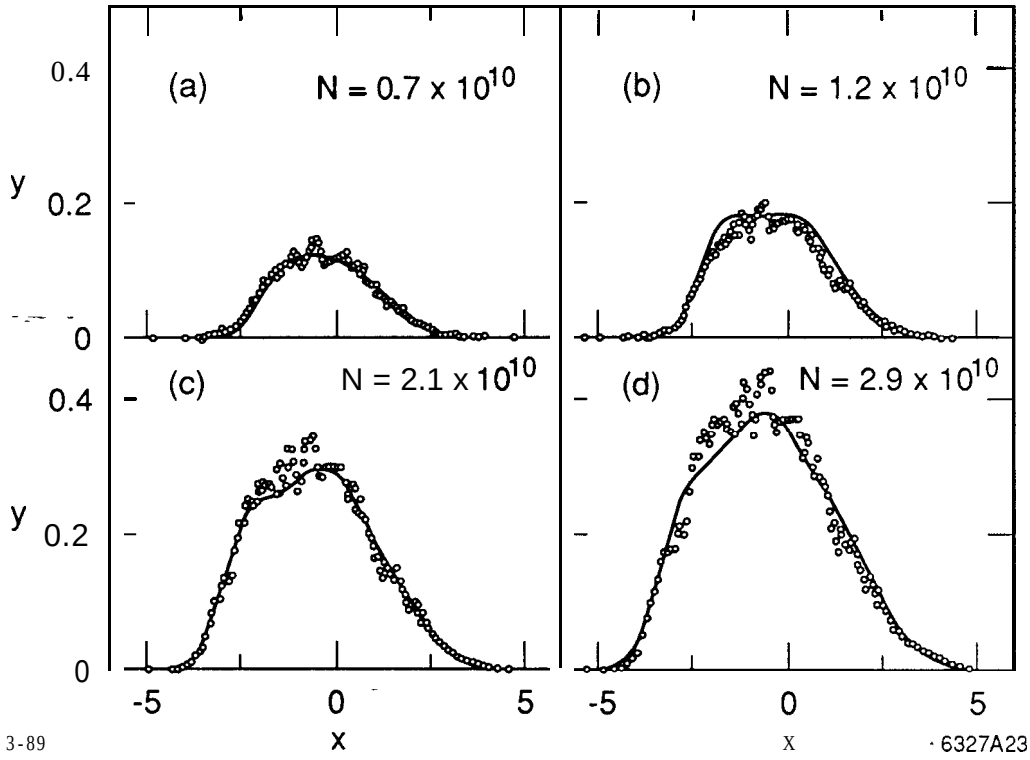

Fig. 28. The calculated damping ring bunch shapes for several current values, when V_{rf} = 0.8 MV. Superimposed on the curves are the measurement results.

with Z_0 = 377 Ω. Superimposed on the curves are the digitized measurement results. The fluctuations in the data (especially at the peaks) are due to nonuniformity in the response of the screen. Considering that there are no fit parameters, the agreement between the data and the calculations is very good. Finally, in Fig. 29 we show the induced voltage v_{ind} and the total voltage v calculated for these same four currents.

4.6.2 *The Incoherent Tune*

For the following calculations let us consider the current N = 1.5 x 10^{10} at v_{rf} = 0.8 MV in the damping rings. Suppose we begin a test particle at rest at position x = $\hat{x}$ in the distorted potential well. Then subsequent oscillations

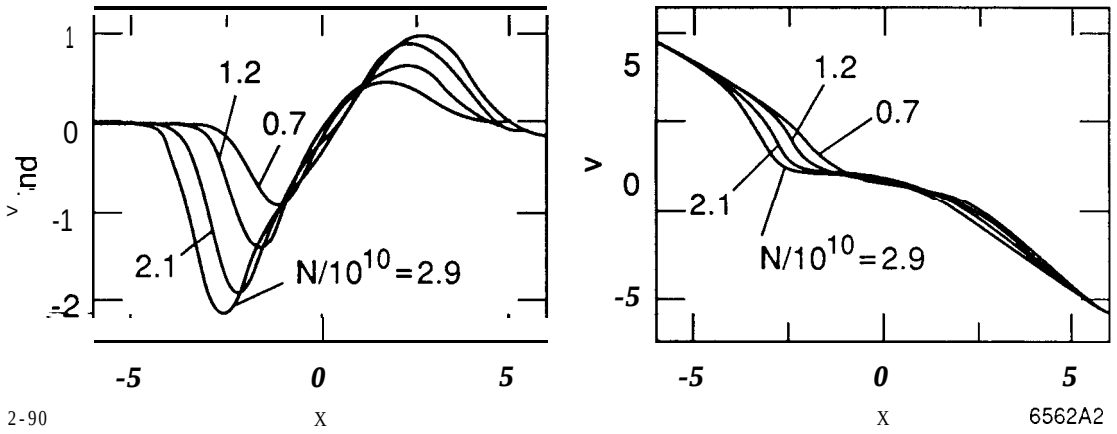

Fig. 29. (a) The induced voltage v_{ind} and (b) the total voltage v = $v_{ind} - x$ when N = 0.7, 1.2, 2.1, and 2.9 x 10^{10} and V_{rf} = **0.8** MV.

within the well are shown in Fig. 30(b), for the cases $\hat{x}$ = -2, -1, 0, 1, and 2. The horizontal axis is the time in units of the nominal synchrotron period. We see quite a variation in oscillation period. The potential well itself is shown in Fig. 30(a); the dashes give the well of the rf alone. Note that $u = 0$, the bottom of the well, is at x = -0.24. Note also that the bottom of the well is not just broadened and that there is an inflection point (u'' = 0) away from the bottom.

For the same current we display, in Fig. 31(b), $\nu(\hat{x})$, for $\hat{x}$ more negative than the position of the bottom of the well. We see that, as with a simple inductive impedance, there is a great tune depression within the bunch. We also note that, as with a simple resistive impedance, the curve has a minimum within the distribution; at the minimum ν = 0.18. In the same frame we display ***v(h).*** [Although ***h*** values up to 10 were included in the calculation, we only show the very beginning of the ***h*** range, in order that the dip in ***v(h),*** near ***h*** = 0.1, can be seen.] At ***h = 0*** the tune is 0.66. In Fig. 31(a)we show the tune distribution. We see that it is broad, centered about ν = 0.7 with a full-width-at-half-maximum of 0.24. Also visible in the plot is a spike, at ν = 0.18, containing very few particle.

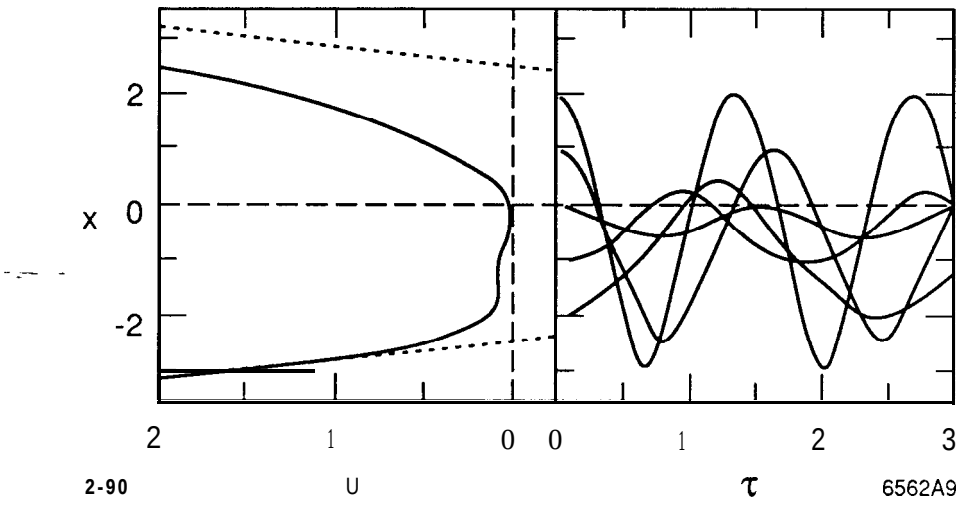

Fig. 30. (a) The potential well and (b) five oscillations within the well when N = 1.5 x 10^{10} and V_{rf} = 0.8 MV.

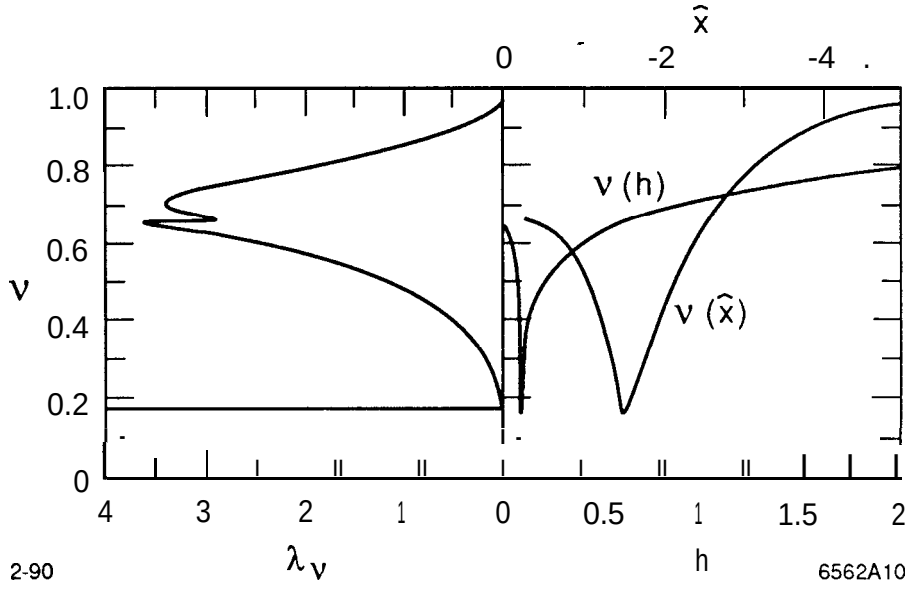

Fig. 31. (a) The tune distribution and (b) the dependence of tune on $\hat{x}$ and h when N = 1.5 x 10^{10} and V_{rf} = 0.8 MV.

In Fig. 32 we characterize the current dependence of the tune distribution by five parameters: $\nu_{.05}$, $\nu_{.25}$, $\nu_{.50}$, $\nu_{.75}$, and $\nu_{.95}$ which signify, respectively, the tune above the first 5%, 25%, 50%, 75%, and 95% of the particles. The region

with dashed curves is the turbulent regime. We see that the tune spread is quite large beyond 5 x 10^9. If we look, for the moment, at the the curve representing the median tune $\nu_{.50}$, we note that it drops most quickly at the beginning of the range, for currents up to 5 x 10^9 and then begins to level off. This general behavior was observed for the quadrupole tune measurements discussed in Chapter 3. In absolute terms, however, the 25% shift shown here at 5 x 10^9 does not agree with the 3 to 4% shift given by the measurements. We believe that this discrepancy signifies that the connection between the coherent quadrupole tune and the incoherent tune of a machine with a broad tune distribution is not so simple.

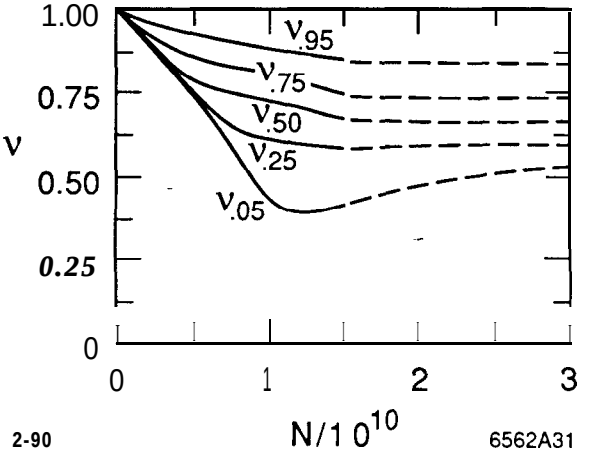

Fig. 32. The current dependence of $\nu_{.05}$, $\nu_{.25}$, $\nu_{.50}$, $\nu_{.75}$, and $\nu_{.95}$ as calculated for the damping rings when V_{rf} = 0.8 MV.

5. CONCLUSIONS

The study of bunch lengthening in the SLC damping rings, described in this paper, can be divided into three parts: the impedance calculations, the bunch length measurements, and the bunch length calculations.

In the paper's first part we described the vacuum chamber geometry of the damping. rings. We introduced a figure of merit for bunch lengthening, the effective inductance ℓ. We found that the ring impedance is dominated by many small,

inductive discontinuities-such as bellows, shallow transition, and masks. There are so many objects that contribute to the total inductance, that if we want to reduce bunch lengthening, we basically need to rebuild the entire vacuum chamber. We ended this part of the paper by computing the wakefield of a very short bunch passing through the entire damping ring, a function that can be used as Green function for the bunch length calculations.

In the paper's second part we described measurements of energy spread, synchronous phase shift, and longitudinal quadrupole tune shift with current that were performed on the SLC North damping ring. We saw that by taking advantage of the unique hardware features found in the SLC it is possible to measure the bunch shape of individual damping ring pulses to good resolution. We found a large amount of bunch lengthening at higher currents; at an rf voltage of V_{rf} = 0.8 MV and bunch population N = 3 x 10^{10} the rms bunch length was doubled. From energy spread measurements we found the threshold current-at the same rf voltage-was 1.5 x 10^{10}.

In the paper's final part we described bunch length calculations that are based on the theory of potential well distortion. We saw, for example, that an inductive machine has lots of bunch lengthening, a resisitive machine little. We saw that in an inductive machine the incoherent tune shift and the tune spread are both large, in a resistive machine they are small. In this chapter we also described a method of extending the potential well calculations into the turbulent regime, once the threshold current for turbulence is known. Then taking the measured threshold value, and using the Green function discussed above, we calulated bunch shapes as function of current. When these shapes were compared with the measured shapes we found excellent agreement. Then finally we computed the tune distribution we expect for the damping rings. As for a purely inductive impedance at higher currents we found the tunes depressed, with the average tune shift large and the tune spread broad.

ACKNOWLEDGMENTS

Credit for the measurements described in Chapter 3 goes to the SLC Damping Rings Commissioning Group, of which the author was but one member. Also, aside from the tune shift calculations, Chapter 4 is based on work that was done with R. Ruth. In addition, the author has profited from discussions with R. Ruth, M. Sands, R. Warnock, T. Weiland, and P. B. Wilson.

REFERENCES

1. L. Rivkin ***et al.,*** Proc. of the 1st European Particle Acc. Conf., Rome, 1988, p. 634.

2. K. Bane, Proc. of the 1st European Particle Acc. Conf., Rome, 1988, p. 637.

3. K. Bane and R. Ruth, Proc. of the 1989 IEEE Particle Acc. Conf., Chicago, 1989, p. 789.

4. T. Weiland, DESY 82-015 (1982) and *Nucl.* ***Inst.*** *Meth.* 212, 13 (1983).

5. K. Bane ***et al.,*** Proc. of the 1st European Particle Acc. Conf., Rome, 1988, p. 878.

6. K. Bane, in ***Physics*** *of* ***High Energy Particle Accelerators,*** AIP Conf. Proc. No. 153 (Am. Inst. of Physics, New York, 1987), p. 978.

7. E. Keil and B. Zotter, ***Particle Accelerators 3,*** 11 (1972).

8. F. Sacherer, CERN Report 77-13, 198 (1977).

9. R. Klatt and T. Weiland, 1986 Linear Accelerator Conference Proceedings, SLAC, p. 282.

10. M. Ross, private communication.

11. L. Rivken ***et al., IEEE Trans.*** *Nucl.* ***Sci. NS-32, No. 5, 2628*** (1985).

12. K. Bane, L. Rivken, and R. Ruth, measurements taken on Nov. 1988 (not published).

13. J. Haïssinski, *Il Nuovo* ***Cimento*** **18B, No.** 1, 72 (1973).

14. A. Papiernik, M. Chatard-Moulin, and B. Jecko, Proc. of the 9th Int. Conf. on High-Energy Acc., SLAC, 1974, p. 375.

15. E. Keil, PEP Note 126, SLAC (1975).

16. K. Bane and P. B. Wilson ***et al., IEEE Trans.*** *Nucl.* ***Sci. NS-24,*** 1485 (1977).

17. K. Nakajima et al., Proc. of the 1st European Particle Acc. Conf., Rome, 1988, p. 570.

18. G. Besnier, "Etude de la Stabilitd d'un Paquet Intense dans l'Anneau ESRF: Effets Longitudinaux," Laboratoire Théorie des Systèmes Physiques, Université de Rennes I (1987).

19. A. Ruggiero et al., IEEE Trans. *Nucl.* Sci. NS-24, No. 3, 1205 (1977).

20. P. B. Wilson et ***al.,*** ***IEEE Trans.*** *Nucl.* Sci. NS-24, No. 3, 1211 (1977).

21. J. M. Wang and C. Pellegrini, Proc. of the 11th Int. Conf. on High-Energy Acc., CERN, 1980, p. 554.

22. D. Boussard, CERN LABII/RF/INT/75-2 (1975).

23. V. K. Neil and A. N. Sessler, Rev. Sci. *Instr.*, 36, 429 (1965).

24. P. B. Wilson, private communication.